LJMU Research Online

Nitschai, MS, Neumayer, N, Häberle, M, Clontz, C, Seth, AC, Milone, AP, Alfaro-Cuello, M, Bellini, A, Dreizler, S, Feldmeier-Krause, A, Husser, T-O, Kacharov, N, Kamann, S, Latour, M, Libralato, M, Van DeVen, G, Voggel, K and Wang, Z

oMEGACat III. Multi-band photometry and metallicities reveal spatially well-mixed populations within ω Centauri's half-light radius

http://researchonline.ljmu.ac.uk/id/eprint/23593/

Article

oMEGACat. III. Multiband Photometry and Metallicities Reveal Spatially Well-mixed Populations within ω Centauri's Half-light Radius

M. S. Nitschai[1] , N. Neumayer[1] , M. Häberle[1] , C. Clontz[1,2] , A. C. Seth[2] , A. P. Milone[3] , M. Alfaro-Cuello[4] ,
A. Bellini[5] , S. Dreizler[6] , A. Feldmeier-Krause[1,7] , T.-O. Husser[6] , N. Kacharov[8] , S. Kamann[9] , M. Latour[6] ,
M. Libralato[10] , G. van de Ven[7] , K. Voggel[11] , and Z. Wang[2]

[1] Max Planck Institute for Astronomy, Königstuhl 17, D-69117 Heidelberg, Germany; nitschai@mpia.de
[2] Department of Physics and Astronomy, University of Utah, Salt Lake City, UT 84112, USA
[3] Dipartimento di Fisica e Astronomia "Galileo Galilei," Univ. di Padova, Vicolo dell'Osservatorio 3, Padova, I-35122, Italy
[4] Facultad de Ingeniería y Arquitectura, Universidad Central de Chile, Av. Francisco de Aguirre 0405, La Serena, Coquimbo, Chile
[5] Space Telescope Science Institute, 3700 San Martin Drive, Baltimore, MD 21218, USA
[6] Institut für Astrophysik und Geophysik, Georg-August-Universität Göttingen, Friedrich-Hund-Platz 1, 37077 Göttingen, Germany
[7] Department of Astrophysics, University of Vienna, Türkenschanzstrasse 17, 1180 Wien, Austria
[8] Leibniz Institute for Astrophysics, An der Sternwarte 16, 14482 Potsdam, Germany
[9] Astrophysics Research Institute, Liverpool John Moores University, 146 Brownlow Hill, Liverpool L3 5RF, UK
[10] INAF, Osservatorio Astronomico di Padova, Vicolo dell'Osservatorio 5, Padova, I-35122, Italy
[11] Université de Strasbourg, CNRS, Observatoire astronomique de Strasbourg, UMR 7550, F-67000 Strasbourg, France
Received 2024 March 28; revised 2024 May 28; accepted 2024 May 29; published 2024 July 26

Abstract

ω Centauri, the most massive globular cluster in the Milky Way, has long been suspected to be the stripped nucleus of a dwarf galaxy that fell into the Galaxy a long time ago. There is considerable evidence for this scenario including a large spread in metallicity and an unusually large number of distinct subpopulations seen in photometric studies. In this work, we use new Multi-Unit Spectroscopic Explorer spectroscopic and Hubble Space Telescope photometric catalogs to investigate the underlying metallicity distributions as well as the spatial variations of the populations within the cluster up to its half-light radius. Based on 11,050 member stars, the [M/H] distribution has a median of (-1.614 ± 0.003) dex and a large spread of ~ 1.37 dex, reaching from -0.67 to -2.04 dex for 99.7% of the stars. In addition, we show the chromosome map of the cluster, which separates the red giant branch stars into different subpopulations, and analyze the subpopulations of the most metal-poor component. Finally, we do not find any metallicity gradient within the half-light radius, and the different subpopulations are well mixed.

Unified Astronomy Thesaurus concepts: Galaxy nuclei (609); Globular star clusters (656); Star clusters (1567)

1. Introduction

Nuclear star clusters (NSCs) are massive and compact star clusters in the innermost region of most galaxies (see, e.g., recent review by Neumayer et al. 2020). They can be found in a wide range of galaxies, with an occupation fraction peaking at galaxy masses in the range 1×10^8 $M_\odot$–1×10^{10} $M_\odot$ (e.g., Sánchez-Janssen et al. 2019; Hoyer et al. 2021). Due to their small sizes (half-light radii of 1–10 pc) and sizable masses (1×10^6 $M_\odot$–1×10^8 $M_\odot$, Georgiev & Böker 2014; Neumayer et al. 2020), they are the densest stellar systems in the Universe, $\geqslant 1 \times 10^6$ $M_\odot$ pc^{-3} (Walcher et al. 2005; Neumayer et al. 2020). Moreover, they have extended star formation histories (Seth et al. 2006; Walcher et al. 2006; Kacharov et al. 2018).

Stripped nuclei are created when smaller galaxies fall into a larger one and are disrupted by tidal forces. During this process they lose most of their stellar content; however, similar to globular clusters, NSCs survive these mergers because they are highly compact and dense. These stripped nuclei will look like massive globular clusters, and hence be able to hide among the globular clusters in a galaxy. Semianalytic models predict 2–6 stripped nuclei in our Milky Way halo (Pfeffer et al. 2014; Kruijssen et al. 2019). One example is M54, the nucleus of the

Sagittarius dwarf galaxy (Alfaro-Cuello et al. 2019, 2020; Kacharov et al. 2022); it was first discovered as a globular cluster until the detection of the remains of the galaxy (Ibata et al. 1994), which has been undergoing tidal stripping over the last several Gyr (Ibata et al. 1997; Laporte et al. 2018).

The most promising other candidate for a stripped nucleus in the Milky Way halo is ω Centauri (ω Cen, NGC 5139), due to the complexity of its stellar populations. It shows multiple sequences in its color–magnitude diagram (CMD; e.g., Anderson 1997; Bedin et al. 2004; Bellini et al. 2010; Milone et al. 2017a) and has a large spread in metallicity (e.g., Freeman & Rodgers 1975; Johnson & Pilachowski 2010). In addition, the internal kinematics of the cluster show the presence of a central stellar disk and a bias toward tangential orbits in the outer parts (van de Ven et al. 2006), counter rotation in the very central region (Pechetti et al. 2024), and fast-moving stars in the inner $3''$ (Häberle et al. 2024b), indicating the presence of an intermediate-mass black hole. In addition, the orbit of ω Cen has been associated with the Gaia-Enceladus merger (Massari et al. 2019; Pfeffer et al. 2021; Callingham et al. 2022; Limberg et al. 2022) ~ 10 Gyr ago (Helmi et al. 2018). The star formation and assembly history of the cluster is still debated and the claims for the age span of its populations vary from 2–3 Gyr (Hilker et al. 2004) up to 4–5 Gyr (Villanova et al. 2007). Other studies have found models fully consistent with a shorter star formation of 1–2 Gyr (Joo & Lee 2013). Finally, tidal material associated with ω Cen is seen directly (e.g.,
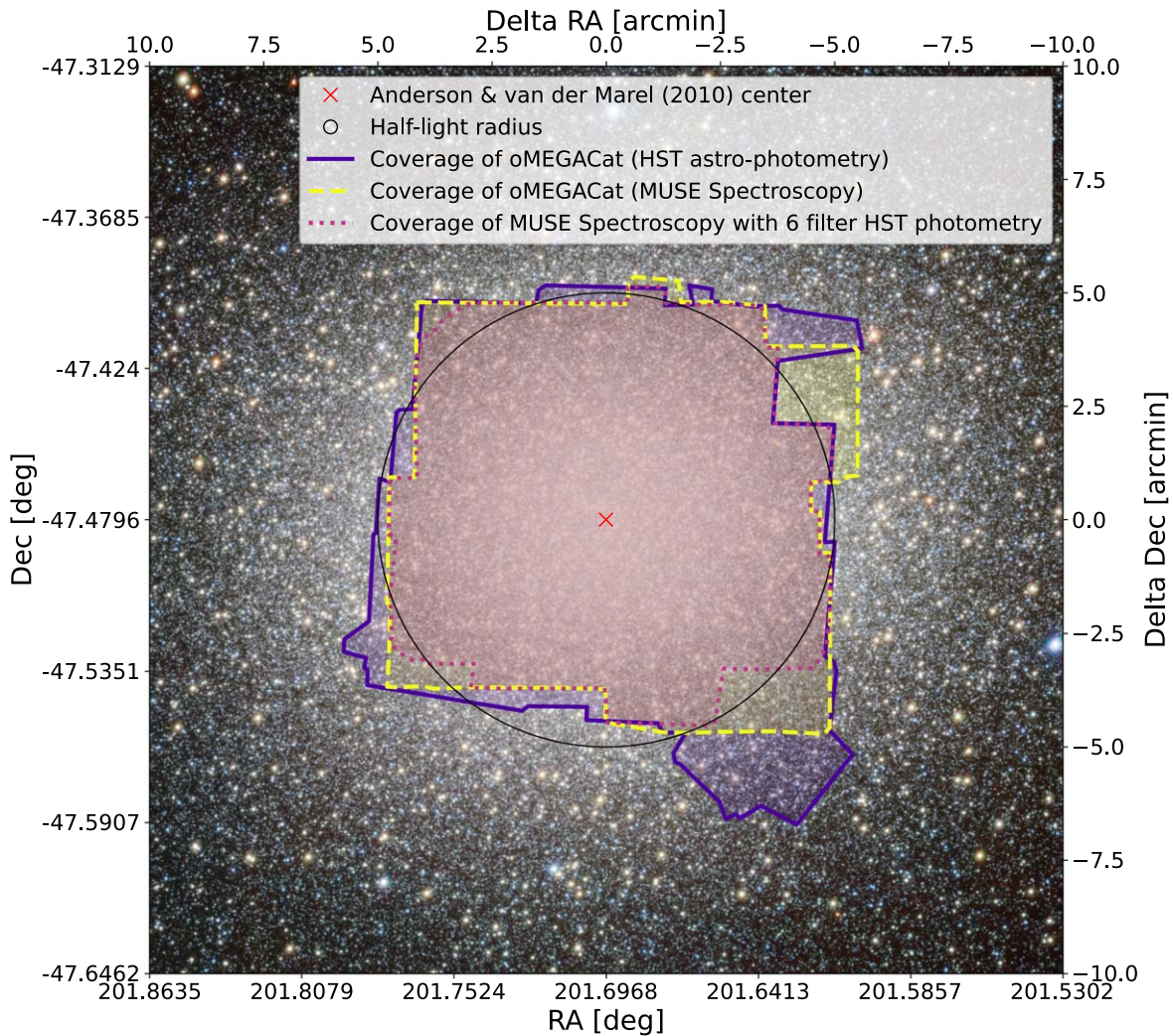
Figure 1. Footprint of data sets. In dark purple with the solid line is the footprint of the new HST catalog (Paper II) and in yellow with a dashed line is the footprint of the MUSE spectroscopic catalog (Paper I). The light purple dotted contours show the area where we have a combined catalog with six-filter photometry from HST. The black circle is the half-light radius at 5′ (Harris 2010) and the red x mark is the Anderson & van der Marel (2010) center. The background is a cutout of a wide-field image taken with the ESO/VST telescope. (Image credit: ESO/INAF-VST/OmegaCAM. Acknowledgment: A. Grado, L. Limatola/INAF-Capodimonte Observatory, https://www.eso.org/public/images/eso1119b/).

Majewski et al. 2012; Ibata et al. 2019, 2023), which further strengthens the stripped nucleus scenario.

ω Cen is the brightest, most massive globular cluster in the Milky Way ($\sim 3.55 \times 10^6 \, M_\odot$, Baumgardt & Hilker 2018). Since it is only at a distance of ~ 5.43 kpc (Baumgardt & Vasiliev 2021), and not heavily obscured by dust (Schlafly & Finkbeiner 2011, $E(B - V) = 0.12$), it provides us with an ideal laboratory to study an NSC. Further, because the masses and star formation histories of NSCs track the galaxies they lived in (e.g., Kacharov et al. 2018; Sánchez-Janssen et al. 2019), and NSCs are much longer-lived than stellar streams, they can also provide us with valuable information about the host galaxy and its merger with the Milky Way.

In our oMEGACat project, we study ω Cen in great detail with the aim of exploring its formation history and interactions with the Galaxy. To do that, we created a spectroscopic catalog (Nitschai et al. 2023, hereafter Paper I) using the Multi-Unit Spectroscopic Explorer (MUSE), and a photometric and astro-metric catalog (Häberle et al. 2024a, hereafter Paper II) using the Hubble Space Telescope (HST) up to the half-light radius of the cluster (see Figure 1 for the coverage of each catalog). In this

work, we make use of these data and investigate the metallicity information we have for the stars in ω Cen. In Section 2 we summarize the observations used to create the catalogs and the quality cuts used in this specific work. Afterward, in Section 3, we present the full metallicity distribution, the chromosome map, and we investigate any possible spatial variation of the metallicity. Finally, in Section 4 we summarize and discuss our findings.

2. Data

2.1. Spectroscopic Data

A detailed description of the spectroscopic data used can be found in Paper I. In summary, the spectroscopic data were acquired with MUSE (Bacon et al. 2010, 2014), a second-generation Very Large Telescope instrument mounted on the UT4 at the Paranal Observatory in Chile and observing in the optical domain (480–930 nm). The observations were carried out between 2021 February and 2022 September in run 105.20CG.001 (PI: N. Neumayer); in addition, we also used the complementary MUSE guaranteed time observations (hereafter "GTO data"). These data together have a full coverage out to

the half-light radius (4.′65 or 7.04 pc, Baumgardt & Hilker 2018) of the cluster.

For the analysis of the data we first extracted the spectra for the individual stars using PAMPELMUSE[12] (Kamann et al. 2013) and the HST catalog from Anderson & van der Marel (2010). Afterward, we used SPEXXY[13] (Husser et al. 2016) to measure the physical parameters of the stars such as effective temperature, metallicity, and line-of-sight velocity. The observed spectra are compared to synthetic spectra from the Phoenix library (Husser et al. 2013) with varying $\log(g)$, $T_{\rm eff}$, and [M/H] while minimizing the χ^2 difference. During the fit with SPEXXY, $\log(g)$ is fixed to the value provided by the isochrone from the PARSEC database (Marigo et al. 2017) that is used to estimate the initial guesses, the α-enhancement is kept constant at $[\alpha/{\rm Fe}] = 0.3$ dex, while $T_{\rm eff}$, [Fe/H], and the line-of-sight velocity are determined.

In addition, we performed multiple tests to check for the robustness of our results, which included an error analysis and membership determination, as well as necessary corrections, such as the atomic diffusion correction. For more details and the spectroscopic data themselves, we refer to Paper I.

2.2. Photometric Data

The detailed description of the photometric data is available in Paper II and here we only briefly summarize it. The astrophotometric part of the catalog is based on observations with the HST spanning over 20 years and using the Advanced Camera for Surveys Wide Field Channel (ACS/WFC) and the Wide Field Camera 3 UVIS Channel (WFC3/UVIS). The data were obtained for various general observing and calibration programs, including a new dedicated program (GO-16777, PI: A. Seth) aimed at providing complementary filter coverage out to the half-light radius and additional epochs required for proper motion measurements. All HST data used for the creation of the astrophotometric catalog can be found under the following DOI in the Mikulski Archive for Space Telescopes (MAST): 10.17909/26qj-g090.

The catalog contains both high-precision photometry spanning from the ultraviolet to the near-infrared and proper motions for around 1.4×10^6 stars. The photometric measurements were performed using techniques specifically designed to analyze crowded environments such as the cores of globular clusters (see Bellini et al. 2017a for details). Six filters have coverage over the full field (ACS/WFC: F435W, F625W, F658N; WFC3/UVIS: F275W; F336W, F814W); in addition, the central region is also covered with multiple epochs of the WFC3/UVIS F606W filter. The proper motions were determined using the technique established and improved in Bellini et al. (2014, 2018) and Libralato et al. (2018, 2022).

In Paper II an empirical correction for spatially dependent photometric variations has been calculated for all seven filters, which is needed due to differential reddening and systematic zero-point variations caused by instrumental effects. Whenever we use this new HST photometry we add the correction for differential reddening and instrumental effects to the magnitudes except where explicitly noted. The coverage for the combined data catalog with six-filter HST photometry is shown in Figure 1.

To combine the photometry from Paper II with the [M/H] values from Paper I, we perform an astrometric crossmatch between the two catalogs using a matching radius of 40 mas (equivalent to approximately one WFC3/UVIS pixel). In addition, we require a magnitude difference in the F625W and F435W filters of $\Delta {\rm mag} < 0.1$ between the new photometry and the Anderson & van der Marel (2010) photometry used for the extraction of the spectra. This leaves us with 307,030 matched stars out of the total of 342,797 from the catalog published in Paper I.

2.3. Quality Cuts

As default, we assume the quality cuts for the spectroscopic catalog described in Paper I, which are given as an extra flag in the catalog ("Flag"). In summary, we use stars with a minimum signal-to-noise ratio (SNR) of 10, >95% membership probability, and with a relative accuracy of recovered magnitude from spectrum extraction with PAMPELMUSE $\geqslant 0.6$. We also exclude stars near the edge of the field (<5 pixel) and where the cross-correlation for the velocity is not reliable. These cuts decrease the number of stars from 342,797 to 156,871. The CMD in the left panel of Figure 2 shows 145,531 stars that fulfill these criteria and are matched to the HST photometry as described in the previous section.

As discussed in Paper I the above cuts are a compromise that allows us to keep a high number of stars with reliable measurements. Since we want to study the metallicity distribution, chromosome map, and spatial variations of subpopulations we want precise and unbiased [M/H] values over our whole field of view. Hence in addition to the default cuts, we use only stars brighter than a general magnitude cut at $m_{\rm F625W} \leqslant 17$. This restriction to bright stars aids in avoiding completeness issues of the spectroscopic data set at fainter magnitudes (see Appendix A), getting higher precision on the [M/H] values with a median SNR of $\sim$54, and removes any [M/H] biases between the different original data sets (GTO, GO, NFM: see Appendix B), which can be caused by different exposure times. To obtain a clean red giant branch (RGB) sample, in a further step, we remove by eye (evolved) blue straggler stars (BSSs) or asymptotic giant branch (AGB) stars. This selection restricts the sample to 11,050 RGB stars (see the right panel in Figure 2).

We do not expect a significant fraction of binaries within our sample. In general, ω Cen has a low binary fraction, only 5% (Elson et al. 1995; Mayor et al. 1996), and even lower in recent work at $2.70\% \pm 0.08\%$ (Bellini et al. 2017b) and $2.1\% \pm 0.4\%$ (Wragg et al. 2024). Therefore, we can safely assume that binaries will not have a significant effect on our results, especially since Wragg et al. (2024) find similar binary fractions for all stellar evolutionary stages using the GTO subsample of the oMEGACat catalog (Nitschai et al. 2023). Only the BSSs show an enhanced binary fraction (>20%). Because of the higher binary fraction among BSSs and the chemically peculiar atmospheres of hot stars due to diffusion (at $T_{\rm eff} \gtrsim 7800$ K, Lovisi et al. 2013), we exclude all stars bluer than the main RGB track (see gray areas in Figure 2).

With these cuts, we get a mean [M/H] error of 0.041 dex. Further, by comparing our MUSE data to the photometric catalog used for the extraction of the spectra (Anderson & van der Marel 2010) we find a completeness >80% in all individual cubes, with a median completeness at 17 mag of 97%. We spatially bin the sample stars and find no significant variation in

---

[12] https://pampelmuse.readthedocs.io/en/latest/about.html
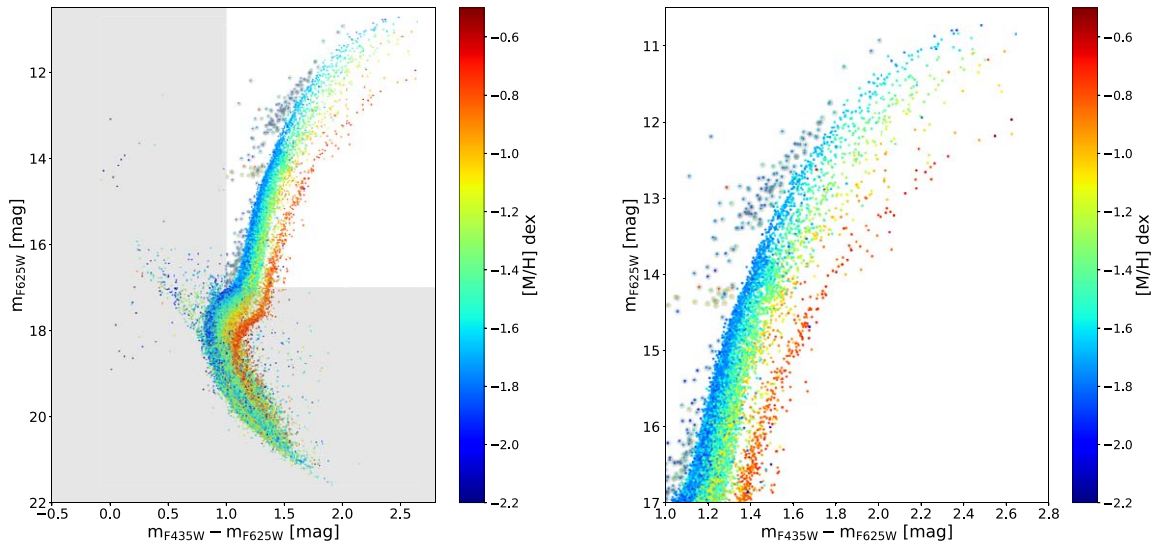[13] https://github.com/thusser/spexxy

Figure 2. Color–magnitude diagrams. On the left is the full CMD of our combined data set color-coded with the metallicity (with 145,531 stars). On the right is a zoom-in on the red giant branch. The gray shaded areas indicate the regions excluded in this work and gray circled dots on the left of the RGB are the excluded AGB and (evolved) BSSs from the RGB sample.

the mean magnitude with radius or at any point within the field of view. This suggests we can make spatial comparisons with minimal concern about instrumental issues.

Note that all metallicities unless otherwise indicated include the atomic diffusion correction; we always use the scaled errors for the metallicity as described in Section 4.2 of Paper I and the new photometry from Paper II.

In the following section, we will investigate the metallicity information we have for the cluster in detail using the above quality cuts. All the data samples described in this section are summarized in Table 1. In Section 3 we will use either the RGB or the RGB phot sample.

3. Results

3.1. Metallicity Distribution

First, we analyze the total metallicity distribution of the 156,871 stars (MUSE QC) passing the default criteria; see the left side of Figure 3. The additional magnitude-cutoff ($m_{F625W} \leqslant 17$ mag) leaves us with 11,050 stars (RGB) and decreases the more extended tail to lower values (below ~ -2 dex), but it also shifts the peak of the distribution to lower values since on average the metal-rich stars have a main-sequence turnoff at fainter F625W magnitudes and hence more metal-rich stars are removed. The cut, however, ensures that both GTO and GO data sets have a similar distribution and no bias is caused due to different data sets; see Appendix B. We also used a kernel density estimator (KDE) to estimate the probability density of the distribution, which we normalized to one to plot it on the same figure. In this distribution multiple peaks are visible and we will identify them later in this section.

The mean [M/H] value is at (-1.550 ± 0.002) dex and the intrinsic standard deviation is (0.255 ± 0.002) dex, which is close to the mean value of the distribution with no magnitude cut (-1.53 dex). The median is (-1.614 ± 0.003) dex with half of the differences between the 16th and 84th percentiles being (0.221 ± 0.003) dex. The median of the overall distribution without a magnitude cut is -1.54 dex, which is closer to the

Table 1
Data Samples

Name	Number of Stars	Description
MUSE	342,797	Spectroscopy Paper I
HST matched	307,030	Spectroscopy with astrophotometry Paper II
MUSE QC	156,871	QC of spectroscopy
HST QC	145,531	HST matched with QC MUSE
RGB	11,050	HST QC and $m_{F625W} \leqslant 17$
RGB phot	10,850	RGB that has a measurement in F625W, F435W, F275W, F336W, and $m_{F814W} \leqslant 17$

Note. QC: quality cuts described in Paper I and the beginning of Section 2.3. The RGB phot sample is needed to have RGB stars in all filters required for the chromosome map; see Section 3.2.1.

mean value since more metal-rich stars are included. All the values and errors (68%) were calculated with bootstrapping.

The range in metallicity for stars brighter than 17 mag reaches from ~ -2 dex to almost -0.5 dex. In detail, 68% of the stars are between -1.77 and -1.33 dex and 99.7% between -2.04 and -0.67 dex. This huge spread in metallicity is, as mentioned previously, an indication of multiple stellar populations, which indeed are visible as distinct sequences in the CMD (see Figure 2).

All our results are comparable to the values in Husser et al. (2020), where in a smaller sample of 1247 stars they found a mean value of -1.50 dex, a median of -1.65 dex, and a range from -1.82 to -1.31 dex for the first and third quartiles. However, since our sample is 10 times larger we have even more accurate values with small uncertainties.

We also used a Gaussian mixture model (GMM) to describe our distributions and the result can be seen on the right side of Figure 3 and in Table 2. We find that the best number of Gaussians to describe the distribution is 11 using the Bayes information criterion (BIC), but eight components would give an almost equally good fit. However, one component is not visible in the figure (index 11 in the table) since it has a very
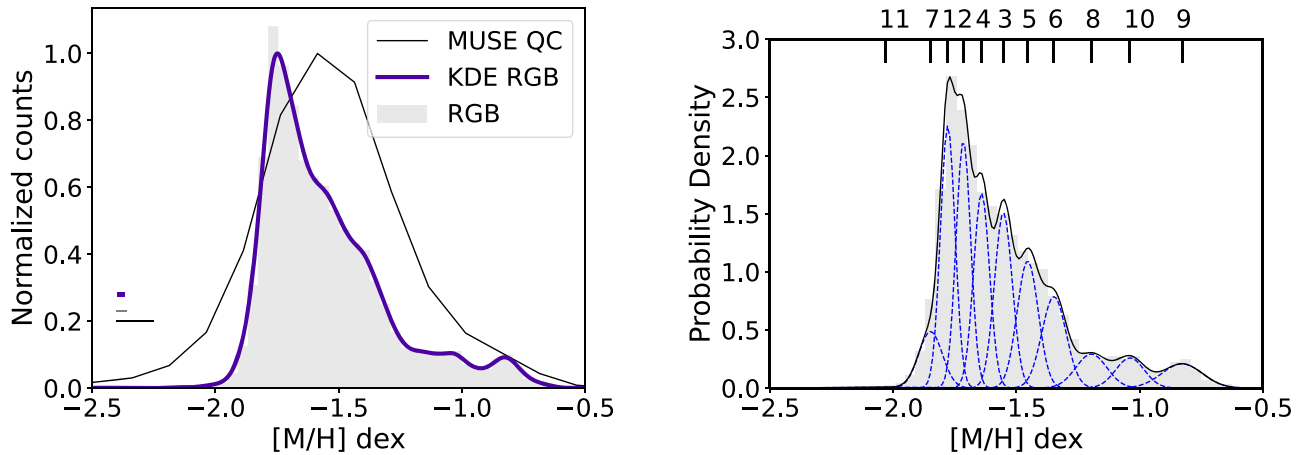
Figure 3. Metallicity distribution. The plot on the left shows the normalized distribution of [M/H] values in the spectroscopic catalog (Paper I) using the default quality cuts in the black line (MUSE QC) and using the extra condition of a minimum brightness of 17 mag in the gray shaded histogram (RGB), and the purple line is the KDE for that distribution. The small horizontal lines on the left side show the bandwidth, 0.030 dex, for the distributions, which are close to the mean errors of the [M/H] values. On the right, we show the same distribution (RGB) as probability density but fitted with a Gaussian mixture model, shown as a black solid line, with each component (11 in total) shown as a blue dashed line. Note that one component has a small amplitude and is not visible in this plot.

Table 2
Multi-Gaussian Components of the Metallicity Distribution

Index #	Mean (dex)	Intrinsic Standard Deviation (dex)	Fraction of Stars (%)
1	−1.779	0.030	18.2
2	−1.715	0.030	16.0
3	−1.553	0.036	13.8
4	−1.642	0.032	13.4
5	−1.454	0.043	11.8
6	−1.348	0.049	9.7
7	−1.849	0.048	4.6
8	−1.196	0.063	4.3
9	−0.828	0.082	4.2
10	-1.039	0.058	3.8
11	−2.033	0.210	0.3

Note. The index # is assigned from the highest to the lowest fraction of stars.

small amplitude compared to the rest and would not count as a separate population but is needed to describe the distribution in the model. Similarly, component 7 is needed for the extended tail toward lower metallicities but together with components 1, 2, and 4 they are not distinguishable by eye in the highest peak of the distribution. Components 3, 8, 9, and 10 can be seen by eye as smaller peaks, and components 5 and 6 are more difficult to distinguish but are still visible.

We have compared our metallicity findings with previous studies already in Paper I where we made a one-to-one comparison. Also, the overall distribution agrees with previous studies (e.g., Johnson & Pilachowski 2010; Mészáros et al. 2021; Alvarez Garay et al. 2024), even though we find more peaks in our distribution. Johnson & Pilachowski (2010) find five peaks in the distribution at −1.75, −1.50, −1.15, −1.05, and −0.75 dex, while Mészáros et al. (2021) and Alvarez Garay et al. (2024) find four peaks, −1.65, −1.35, −1.05, and −0.7 dex, and −1.85, −1.55, −1.15, and −0.80 dex respectively. All these peaks are in agreement with at least one of our peaks within the 3σ range. The difference in the number of peaks can be explained due to the difference in the data, specifically the number of data, since it can make it difficult to identify and separate peaks in the distribution with a lower number of stars.

All the above-mentioned studies have stars that reach larger radii than ours, but they have fewer than 1000 stars, while we have more than 10 times their number, which allows us to distinguish different metallicity components more easily. However, even in our case, one could reduce the number of components to five if one only looks at the distribution by eye, since peaks 1, 2, 4, and 7 can be taken as one, and the peaks of components 5 and 6 or 8 and 10 are not that clearly visible in the overall distribution, and component 11 is not visible at all. Even with the GMM, we can see that eight components would give an almost perfect fit to the distribution and that small variations in the sample of stars can also change the preferred number of Gaussians. This demonstrates the advantage of our huge data set, which allows for much more detailed studies and analysis.

Husser et al. (2020) identify nine subpopulations and give their mean metallicity values. Our multi-GMM does not separate the stars in different subpopulations, since also photometric analysis needs to be taken into account. However, we can compare their positions on the chromosome map in Section 3.2.1 and identify which component belongs to which subpopulation (P) identified in Husser et al. (2020). P1, P2, and P3 (mean [Fe/H] = −1.83, −1.80, −1.74 dex) would correspond to our components 7, 1, and 2, P5 (−1.24 dex) to component 6, and P8 (−1.50 dex), P6 (−1.47 dex), and P4 (−1.50 dex) to components 3 and 5. Our component 6 could be part of P4 or P3. From the chromosome map, we can identify component 9 as P7 (−0.18 dex) and components 10 and 8 as P9 (−0.72 dex) but the metallicity values disagree the most with our findings. However, they have a lot fewer stars than we have, especially since their P7 and P9 are not well populated. With our data, they can be much better studied and separated. In the following sections, we investigate different subpopulations a bit further. We do not aim to precisely separate and identify all subpopulations in detail; this will be done in future work (C. Clontz et al. 2024, in preparation). Nevertheless, this analysis already shows how our huge data set can improve studies of subpopulations.

Lastly, Johnson et al. (2020) find two very metal-poor populations, below −2 and −2.25 dex. Our component 11 contains 30 stars at the very low end of the metallicity distribution, reaching as low as −2.738 dex and as high as −1.990 dex, but only four stars above −2.25 dex. However,
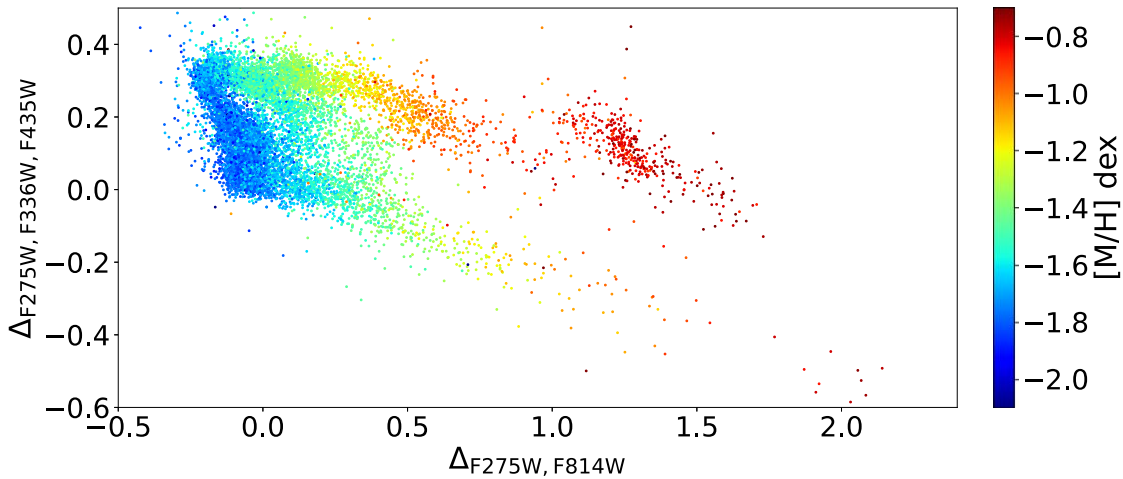
Figure 4. Chromosome map of ω Cen color-coded with metallicity. One can identify different subpopulations in the map, but since we do not aim to separate them precisely in this work we also do not draw the line separating first- and second-generation stars as is usually done in globular clusters.

this component is just a tiny fraction of the whole sample and its stars do not cover the whole CMD range (most of them lie close to magnitude 17 mag), indicating that they are not a separate population and are not the same stars as in Johnson et al. (2020), where most of these stars lie on the brighter RGB. Hence, our stars in component 11 are individual stars with special [M/H] values either due to measurement problems or because they could be binary stars. Overall, we can conclude that we do not find the most metal-poor population from Johnson et al. (2020) in our sample, even though we have a few low-metallicity stars.

3.2. Photometry and Metallicity

3.2.1. Chromosome Map

In this subsection, we focus again on RGB stars with $m_{F625W} < 17$ mag. In addition, we require the stars to have accurate photometric measurements in five different HST filters (F275W, F336W, F435W, F625W, and F814W) in the photometric catalog of Paper II. These requirements leave us with a sample of 10,850 stars (RGB phot).

Almost all globular clusters host significant spreads in light-element abundance within them, following a basic pattern: a population with abundances akin to field stars, and one or more anomalous populations, with varying enrichment in some elements (e.g., He, N, Na) and depletion in others (e.g., C, O), but the specifics of each cluster are unique (see the review by Bastian & Lardo 2018). These spreads in abundance are typical for old and massive clusters and are known as multiple populations. However, abundance variations in Fe and heavy elements are rare and have only been detected in more complex clusters such as ω Cen (Willman & Strader 2012).

The chromosome map is a photometric diagram used to identify multiple stellar populations in globular clusters. It uses multicolor photometric information that is sensitive to element abundance variations to characterize the presence and diversity of multiple populations (Milone et al. 2017b). Many studies have provided accurate investigations of the subpopulations of ω Cen (e.g., Tailo et al. 2016; Husser et al. 2020; Latour et al. 2021). Here, we take advantage of an unprecedented data set that comprises photometry and spectroscopy of more than 10,000 RGB stars to better investigate them.

To construct the chromosome map, we follow the technique from Milone et al. (2017a) and use the filters F814W, F336W, F275W, and F435W. Milone et al. (2015a, 2015b) showed that the combination of the pseudo-color $C_{F275W,\ F336W,\ F438W}$ (in our case $C_{F275W,\ F336W,\ F435W}$) (Piotto et al. 2015) with the $m_{F275W} - m_{F814W}$ color maximizes the separation between stellar populations along the main sequence (MS) and the RGB. Here we analyze only the RGB populations, deferring a more comprehensive view of subpopulations and their exact separation in the cluster to a later paper (C. Clontz et al. 2024, in preparation).

In detail, the pseudo-color $C_{F275W,\ F336W,\ F435W}$ is selected since it is sensitive to the degree of CNO processing in the multiple populations. This is thanks to the fact that the F275W filter includes the OH molecular band, the F336W the NH band, and the F435W the CH and CN bands (e.g., Milone et al. 2015a). Simultaneously the F275W and F814W filters provide a wide color range, being sensitive to the effective temperature and thus to different metallicities or helium abundances, since helium-enhanced stars are hotter at the same luminosity (e.g., Milone et al. 2012, 2015a).

The detailed steps to calculate the Δ values can be found in Appendix C. In general, the following relations are used:

$$\Delta_{F275W,F814W} = W_{F275W,F814W}$$
$$\times \frac{X - X_{fiducialR}}{X_{fiducialR} - X_{fiducialB}} \qquad (1)$$

and

$$\Delta_{F275W,F336W,F435W} = W_{F275W,F336W,F435W}$$
$$\times \frac{Y_{fiducialR} - Y}{Y_{fiducialR} - Y_{fiducialB}} \qquad (2)$$

with fiducialR the redder fiducial line and fiducialB the bluer line in color space. Further, $X = m_{F275W} - m_{F814W}$, $Y = C_{F275W,\ F336W,\ F435W}$, and the pseudo-color $C_{F275W,\ F336W,\ F435W} = (m_{F275W} - m_{F336W}) - (m_{F336W} - m_{F435W})$. The final chromosome map is shown in Figure 4. The few stars lying on the very blue side of the chromosome map are most likely remaining evolved BSSs or/and binaries (see Marino et al. 2019b; Kamann et al. 2020; Martins et al. 2020) that have not been removed from our RGB sample because they lie close to the bluest RGB stars.
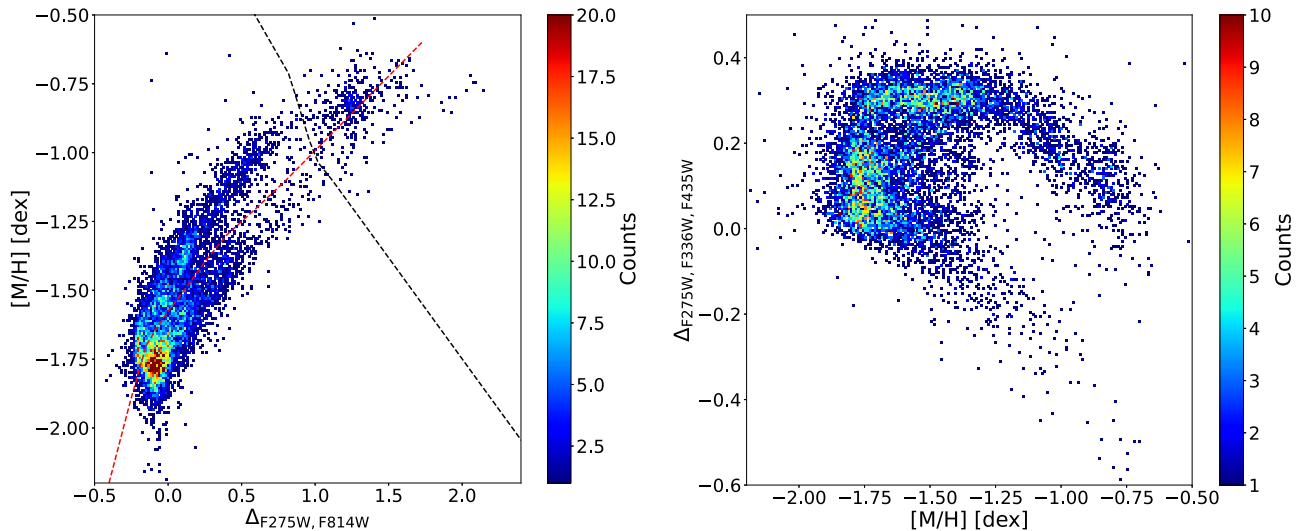
Figure 5. Δ values as a function of [M/H]. The chromosome Δ values—metallicity against $\Delta_{F275W,F814W}$ (left) and $\Delta_{F275W,F336W,\ F435W}$ plotted against metallicity (right)—in a density histogram. On the left, the red line separates the two streams visible and the black dashed line indicates the metal-rich stars that are excluded from the analysis in Section 3.4.3.

Including the bright (evolved) BSSs (gray shaded points in Figure 2) would create a more extended tail to bluer $\Delta_{F275W,F814W}$ values in the chromosome map.

The x-axis of this chromosome map is mostly sensitive to stellar populations with different helium (He) content and metallicity (Fe), whereas the y-axis is mostly efficient in identifying stellar groups of stars with different nitrogen (N) abundance (see, e.g., Figures 25 and 27 in Marino et al. 2019a and Figure 5 in Milone et al. 2020, for details). In a typical globular cluster, what is known as first-generation (1G) and second-generation (2G) stars would lie around $\Delta_{F275W,F814W} \sim 0$, with the 1G being centered at the origin (0, 0) and the 2G stars found above ($\Delta_{F275W,F336W,\ F435W} > 0$). In ω Cen the most metal-poor stars follow this pattern, while higher-metallicity stars have different tracks at $\Delta_{F275W,F814W} > 0$. Further abundance studies will help us distinguish the different subpopulations even better.

3.2.2. Metallicity Dependence

Since we have the metallicity information for all these stars we can investigate the relationship between the Δ values and [M/H]; see Figure 5. $\Delta_{F275W,F336W,\ F435W}$ versus [M/H] shows, as expected, a similar structure to the chromosome map since $\Delta_{F275W,F814W}$ tracks the [M/H] variations. Specifically, [He/H] and [Fe/H] variations are the main cause of the horizontal displacement in the chromosome map (see Figure 5 in Milone et al. 2020 and Figure 27 in Marino et al. 2019a).

Interestingly, we notice two distinct sequences or streams in the $\Delta_{F275W,F814W}$ versus [M/H] diagram, which correspond to stars with different light-element abundances (see also Figure 11 in Section 3.4.3). Specifically, the upper stream is composed of stars with the most extreme chemical properties, enhanced in [Na/Fe] and [Al/Fe] and depleted in [O/Fe] and [C/Fe] with respect to stars in the lower stream with the same metallicity (Marino et al. 2019a; Milone et al. 2020). It is also known that the vertical displacement in the chromosome map is mainly caused by [N/Fe] (e.g., Marino et al. 2019a; Milone et al. 2020), hence stars located in the upper stream have higher [N/Fe] abundance than stars in the lower stream. In addition, He-enhanced and Mg-depleted stars are expected in the upper

stream (Milone et al. 2015b, 2018, 2020; Marino et al. 2019a). Further, Fe enrichment occurs in both streams: the upper has a slightly higher peak (Marino et al. 2019a), which we will also show in Sections 3.2.3 and 3.4.3.

In the future we are aiming to perform a detailed study on the abundances of individual stars (Z. Wang et al. 2024, in preparation) using DD-Payne (Ting et al. 2017; Xiang et al. 2019) and to further investigate the effect the abundance variations have on the chromosome map. That will allow us to identify the main cause of the two sequences seen in the left panel of Figure 5. We are also working on combining stellar spectra of the same subpopulations to identify the overall abundance differences between subpopulations (S. Di Stefano et al. 2024, in preparation), which will also help us tackle the cause of the two sequences.

3.2.3. The Metal-poor Component and Its Multiple Populations

The most metal-poor stars ([M/H] $\lesssim -1.60$ dex) of the cluster follow a similar trend to the stars of monometallic globular clusters that separate into the so-called 1G and 2G stars along the $\Delta_{F275W,F336W,\ F435W}$ axis due to light-element variations.

To identify these metal-poor stars in the chromosome map, we used stars in the most metal-poor components of the GMM (index # 1, 2, 4, 7, 11). Each star is assigned to the component that makes the greatest contribution to the GMM at the star's metallicity. This creates sharp metallicity cutoffs for the GMM populations. Then we remove blue or red outliers in the chromosome map (see the left panel in Figure 6) for the remaining stars.

If we only look at those stars, we can see that they also have a spread in metallicity reaching from -1.82 to -1.68 dex for 68% of the stars; see Figure 6. With a simple GMM fit we identify three peaks (using the BIC) in the $\Delta_{F275W,F336W,\ F435W}$ distribution, separating them into three different populations. We see that the third peak (highest $\Delta_{F275W,F336W,\ F435W}$ values) has the highest metallicity (similar to the findings in Marino et al. 2019a) and that all have a significant width. We investigate that further by looking at their metallicity distribution. The yellow peak has the highest mean metallicity at -1.721 dex and an intrinsic standard deviation of $\sigma = 0.065$ dex, the red one is at -1.762 dex and $\sigma = 0.071$ dex, and the black one is at
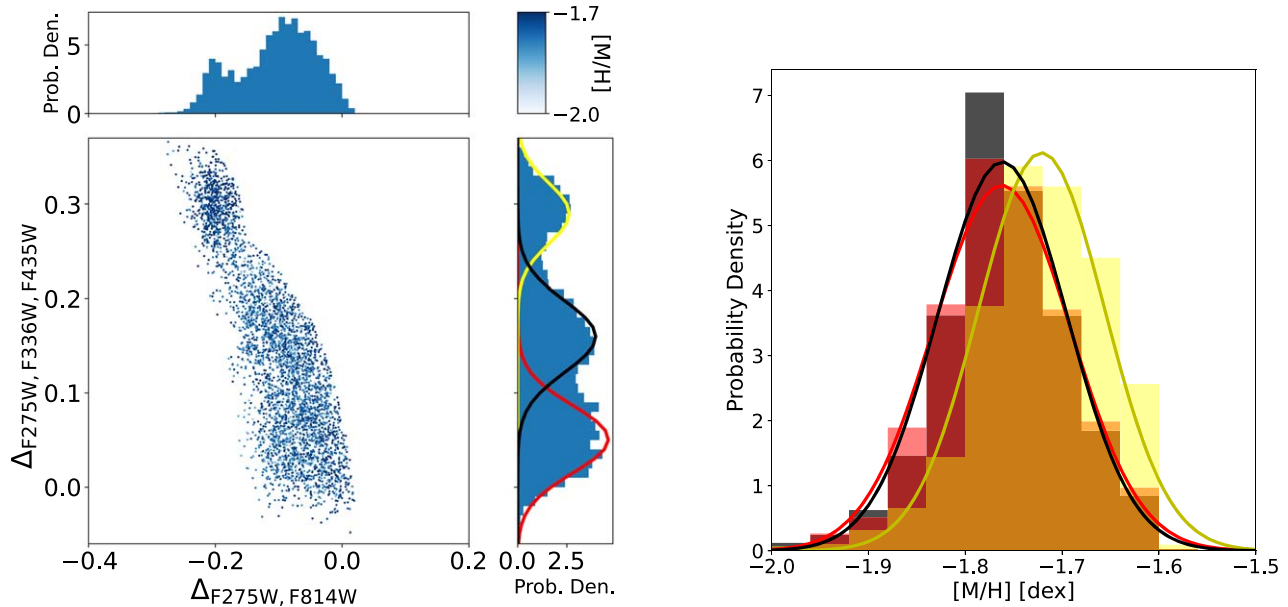
Figure 6. Multiple populations in the metal-poor stars. On the left is the chromosome map for only the metal-poor stars with the probability density histograms of the Δ values. There we can identify three peaks in the $\Delta_{F275W,F336W,\,F435W}$ histogram and plot their metallicity distributions on the right. The metallicity distributions for the populations indicated with the red and black lines are very close, while the population plotted in yellow exhibits a higher metallicity.

-1.762 dex and $\sigma = 0.067$ dex. They have similar standard deviations and [M/H] but the yellow peak is offset to higher [M/H], with a p-value below 1% for the Anderson–Darling and Kolmogorov–Smirnov tests. The red and black distributions have higher p-values $> 25\%$, meaning that they are consistent with being drawn from the same distribution. Overall, even in this one metallicity component, there is a spread in [M/H] and we find higher [M/H] for higher $\Delta_{F275W,F336W,\,F435W}$ values, as seen also in Marino et al. (2019a). However, since the difference is small, even though it seems to be significant (see also Figure 9), we do not have pure iron abundance but [M/H], which could be increased with enrichment in Na and Al, which is expected for the black peak and even more strongly for the yellow one.

Higher $\Delta_{F275W,F336W,\,F435W}$ also mean more enhanced Na and Al abundances and depletion in O and Mg, as explained in Section 3.2.2, and hence more He-rich stars (Milone et al. 2015b, 2018; Marino et al. 2019a). Therefore we will call stars belonging to the red peak an Na-poor metal-poor (Na-poor MP) population and those belonging to the yellow peak an Na-rich metal-poor (Na-rich MP) population, and in the black peak are stars with intermediate Na enrichment.

There have been studies identifying subpopulations in ω Cen on the RGB (e.g. Lee et al. 1999; Pancino et al. 2000; Sollima et al. 2005; Husser et al. 2020) and the MS (e.g., Bedin et al. 2004; Bellini et al. 2010; 2017b; Milone et al. 2017a). However, connecting the RGB and MS stars into the same subpopulations is a complex task that has not been done so far since the subpopulations overlap and cross each other below the turnoff point in the CMD. This will be the focus of future studies (C. Clontz et al. 2024, in preparation).

3.3. Spatial 2D Metallicity Distribution

We analyze the 2D spatial distribution of the metallicity since 2D variations might average each other out in radial bins.

We create smooth maps that still show details using the median of the 200 nearest neighbors (see Figure 7) and for

visualization only the locally weighted regression (LOESS) technique (with a regularization factor $f = 0.1$, Cappellari et al. 2013). We choose 200 nearest neighbors since that gives a smooth map without patches also in the velocity (similar to Pechetti et al. 2024). In Figure 7 we can see that indeed there is some structure, almost ring-like, consistently visible in both the LOESS and median maps. In addition, we also plot half the difference of 68% of the 200 nearest neighbors as an indication of the dispersion of the [M/H] values. Regions with lower median metallicity in the outskirts of the field have a relatively narrow metallicity distribution, while some of the structures with higher median metallicity also have a higher dispersion. However, there are also regions with moderately high median [M/H] and a narrow [M/H] distribution. In general, the variation in the dispersion map does not perfectly match the ring-like structure of the median metallicity map. Further, the pattern does not follow the MUSE pointing structure, reassuring us that the structure is not caused by calibration differences. We also verified that the structure does not appear if we take the ratio between the redmost RGB branch (metal-rich stars) and the blue RGB (metal-poor stars), which suggests that the structure is not caused by biases in our observations or selection of the sample in specific regions. However, this also indicates that the structure is not caused by the most metal-rich population but by some other intermediate [M/H] populations that might have been accreted later in the evolution of the cluster and is not yet well mixed.

3.4. Metallicity Gradients

3.4.1. Overall Cluster Gradient

Since the cluster is elongated in the plane of the sky, we do not use circular radial bins for further analysis but elliptical bins. We use $100°$ for the positional angle (van de Ven et al. 2006; Kamann et al. 2018), 0.07 for the ellipticity (median value from Geyer et al. 1983; Pancino et al. 2003; Calamida et al. 2020, inside 5′) and the equivalent radii for the bins are

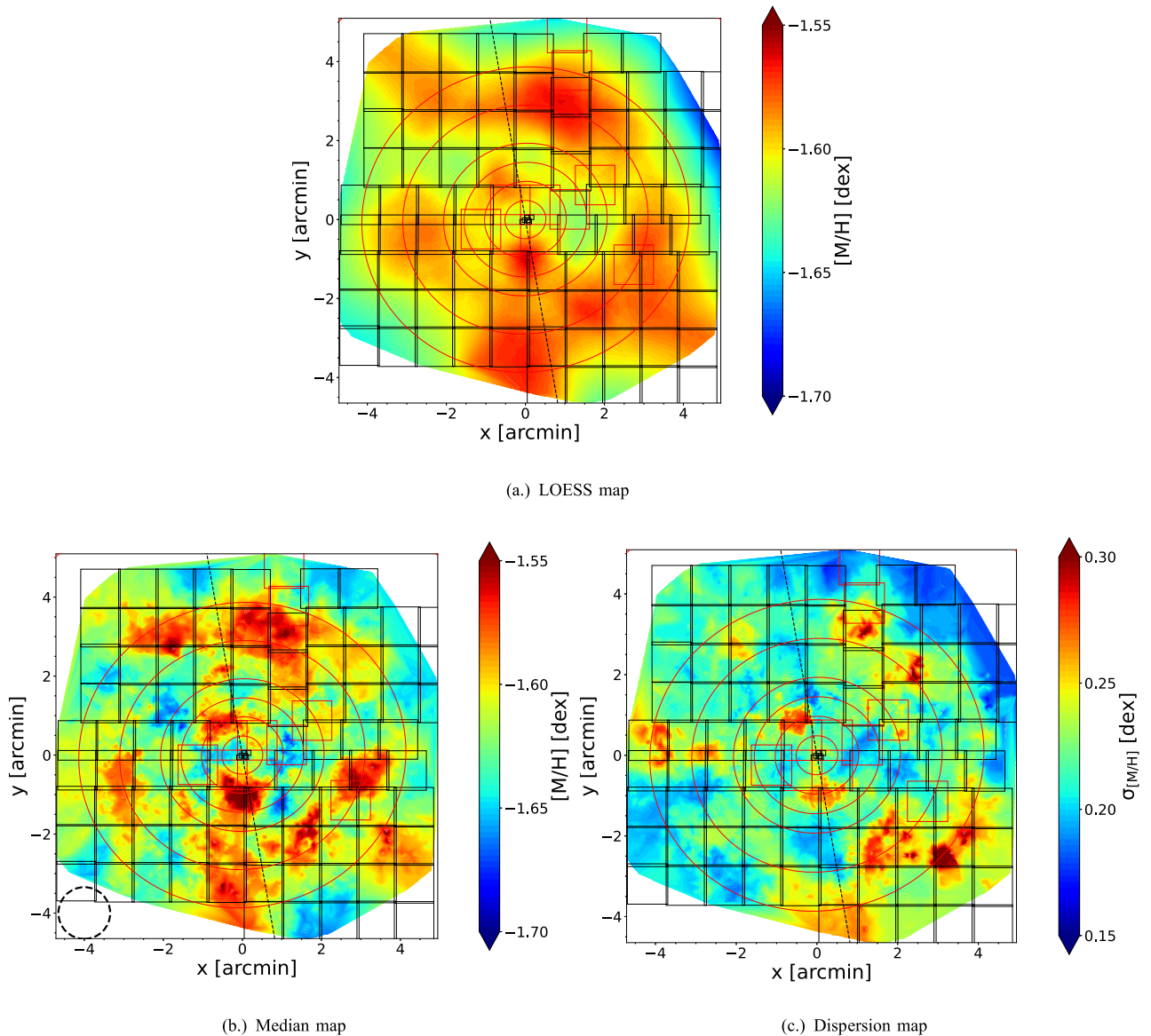(a.) LOESS map

(b.) Median map

(c.) Dispersion map

Figure 7. Metallicity maps. (a) The LOESS smoothed metallicity map for visualization only, (b) the median map from the 200 nearest neighbors, and (c) the 68% dispersion map from the 200 nearest neighbors. In (b) the black dashed circle in the left corner shows the mean radius of the 200 neighbors. The pointing structure from MUSE is shown with faint squares, the red elliptical annuli are the bin edges used in Section 3.4, and the minor axis of the elliptical annuli corresponding to the rotation axis is shown as a black dashed line.

(0.5, 1, 1.5, 2, 3, 4, 7) arcmin. These bin edges are overplotted in red in Figure 7. In all the following analyses we calculate the median circular radius in each of the elliptical bins and show that in the figures.

In Figure 8 we plot the mean and median metallicity values for each bin with the 99.7% as 3σ error bars, derived with bootstrapping. We can conclude that there is no significant gradient within the half-light radius of the cluster. However, there is an indication of the ring we see in the 2D distribution (Section 3.3), in the bins between $2'$ and $4'$, where the median [M/H] is almost 3σ (99.7%) above the global median [M/H] of the cluster. Also, the last bin lies just outside the 3σ range below the overall median value. We see these same trends in the mean metallicity profile. The trend is not as strong as in the 2D maps since it is not a perfect ring and some lower and higher [M/H] areas cancel each other out when looking at the radial profile, but the signature is still visible.

Previous studies (e.g., Sollima et al. 2007; Bellini et al. 2009; Calamida et al. 2017, 2020) find spatial differences in subpopulations of the MS and the RGB. The bluer MS (associated with the intermediate-metallicity RGB by Piotto et al. 2005), which is thought to be He-enriched (Bedin et al. 2004; Norris 2004; Piotto et al. 2005) is more centrally concentrated than the red MS (associated with the metal-poor RGB) but increasing toward the outer parts, above $25'$. For the RGB the rich and intermediate populations follow the same distribution and are more centrally concentrated with a decline toward $8'-10'$ (Bellini et al. 2009). The last bin in our metallicity gradient and lower metallicity toward the outer parts of the 2D map (see Section 3.3) indicate a similar trend with the more metal-rich or intermediate populations declining at the edge of the half-light radius. Calamida et al. (2017, 2020) show that the more metal-poor stars follow the cluster elongation and are more numerous in the northern half, while the more metal-
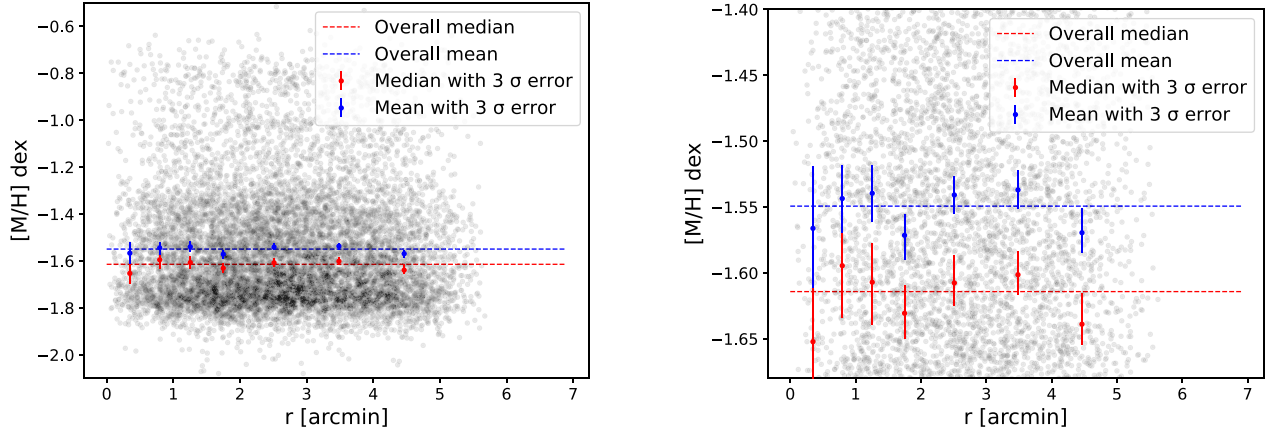
Figure 8. Overall metallicity gradient. Black are all the stars used for this analysis, red is the median value for each bin, and blue is the mean value. The dashed lines show the total median or mean value for the whole sample. The left panel shows the whole [M/H] range while the right panel is a zoom-in to metallicities around the mean and median.
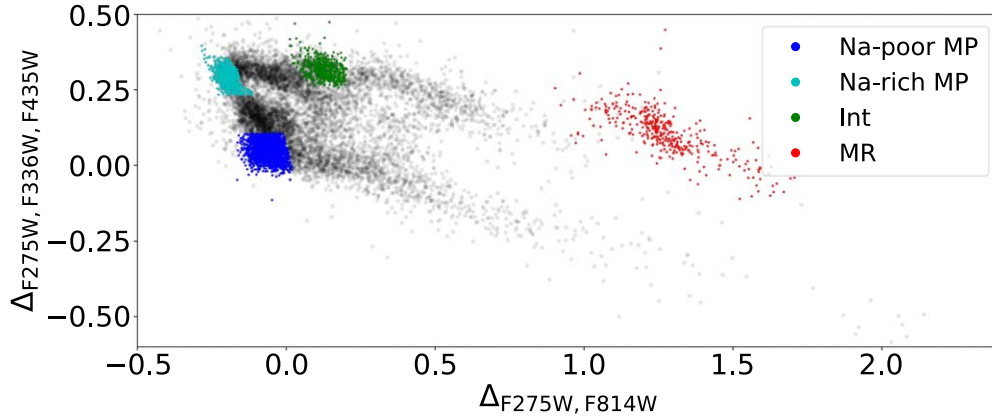

Figure 9. Chromosome map showing the four different subgroups considered in Section 3.4.2. Red are the metal-rich stars, green the intermediate population, cyan the metal-poor but Na-rich, and blue the metal- and Na-poor stars.

rich are elongated in the northeast–southwest direction and are more numerous in the eastern half. This trend is not visible in our data in the 2D distributions.

In general, for all these previous studies the spatial differences are prominent at the edge or after the half-light radius, which is outside our data range. From our analysis, inside the half-light radius, the subpopulations seem to be well mixed in radial bins.

3.4.2. Spatial Differences between Subpopulations

Further, we want to investigate whether there is a difference in the spatial distribution of different subpopulations. To this aim, we use four different subgroups, identified from the GMM and the chromosome map as follows. Na-rich but metal-poor (Na-rich MP), Na-poor, and metal-poor (Na-poor MP) populations were identified in Section 3.2.3, then we further select one intermediate-metallicity (Int) population, index 7 in the GMM, and constrain it to the stars belonging to the clear overdensity in the chromosome map. We emphasize, however, that this is not the only intermediate-metallicity population but one of many, and we only selected this one because it is easily distinguishable in the upper sequence of the chromosome map. Finally, the metal-rich population (MR) includes the most metal-rich stars with a visible separate sequence in the chromosome map. See Figure 9 for their location on the chromosome map.

This identification of four subpopulations is a first selection of some easily detectable subpopulations in the chromosome map that span a wide spread in [M/H] and are far apart in the chromosome map. We do not aim to find all subpopulations but to select a few to check their distribution over the field of view. We plan to use all available information and machine learning techniques to classify the subpopulations in an upcoming paper (C. Clontz et al. 2024, in preparation).

The cumulative radial distribution and metallicity gradient of each subpopulation are shown in Figure 10. The Anderson–Darling test gives a p-value higher than 25%, so the null hypothesis is not rejected and the subpopulations could have the same underlying distribution. The only exception is between the Na-poor MP or Na-rich MP and the Int populations, where the p-values are lower ($\sim$8%) but still too high to reject the null hypothesis. Future more detailed separation between subpopulations might reveal stronger differences. The populations do not show any significant metallicity gradient; see Figure 10 right panel. The right panel also confirms our finding in Section 3.2.3 that the metallicity difference between Na-rich and Na-poor metal-poor populations is significant (outside the 3σ range) for all radii, except for the first bin, where due to the low number of stars the error bars are larger. The subpopulations, depending on metallicity or Na enrichment, we selected are all well mixed.
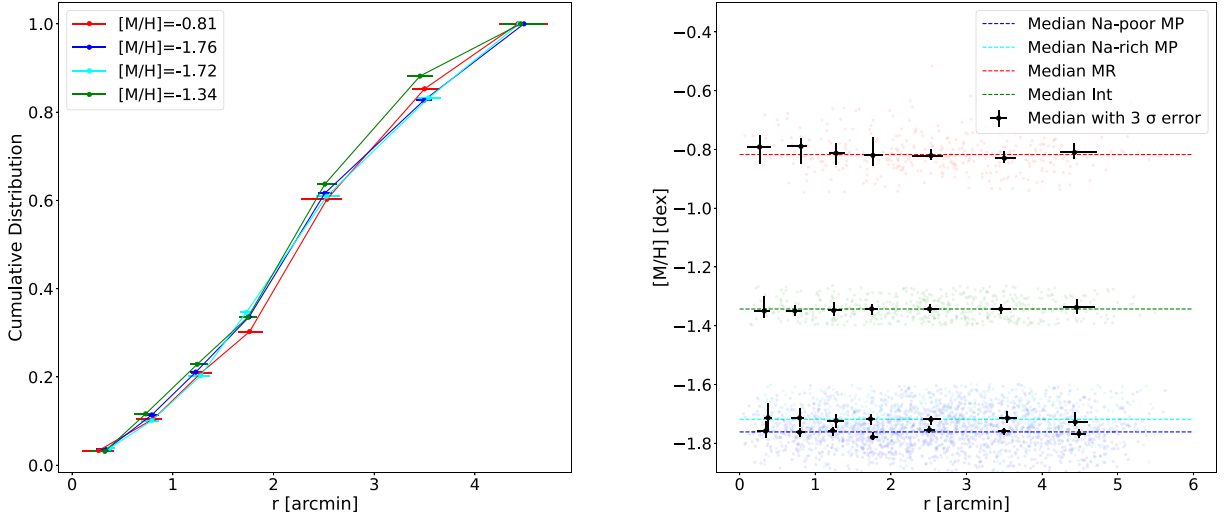
Figure 10. Spatial distribution of the subgroups. The left panel shows the cumulative distribution of the four subgroups; the labels show the median [M/H] value. On the right is their metallicity vs. radius.
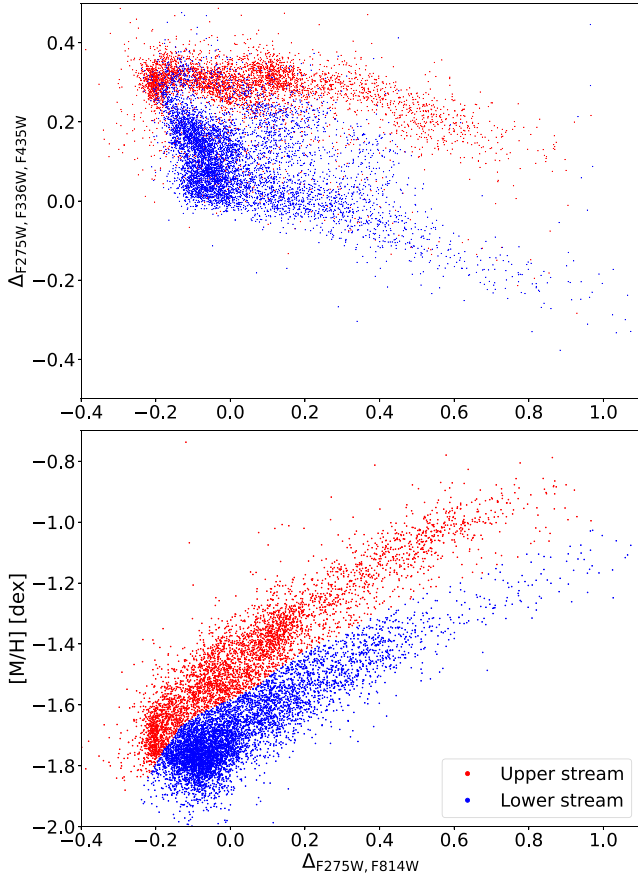

Figure 11. The two streams in [M/H] vs. $\Delta_{F275W,F814W}$. The top panel shows the chromosome map and the bottom panel $\Delta_{F275W,F814W}$ vs. [M/H]. We color-coded the stars depending on whether we identified them as belonging to the upper or lower stream in the original Figure 5.

3.4.3. Differences in the Two Streams of [M/H] versus $\Delta_{F275W,F814W}$

In the previous section, we chose four subpopulations with different metallicities and Na enhancements and found no significant spatial difference. To further check the difference between subpopulations with different enhancements in light

elements, we use the two streams seen in [M/H] versus $\Delta_{F275W,F814W}$ (see Section 3.2.2 and Figure 11). We exclude the metal-rich stars (black dashed line in Figure 5) since they lie in between the sequences. The cumulative distribution is shown in the left panel of Figure 12 and the two streams do not differ significantly. Kolmogorov–Smirnov and Anderson–Darling tests show p-values of 10% and 8%, confirming that the null hypothesis is not rejected for their spatial distribution. However, the p-values are lower than for the subpopulations, indicating that there might be differences that could get stronger toward larger radii (similar to the difference in the blue and red MSs, Sollima et al. 2007; Bellini et al. 2009).

The metallicities of the two streams, however, are different, with the upper sequence having a median metallicity higher than the lower sequence. That is not unexpected since most of the metal-richer stars lie on the upper stream and slightly higher iron values are expected in that stream as discussed in Section 3.2.2. However, again no significant metallicity gradient is visible (see right panel in Figure 12).

4. Conclusion

We present a detailed study of the metallicity distribution of 11,050 RGB stars in ω Cen with a mean error of 0.041 dex and a median SNR $\sim$ 54. We find a mean value of -1.550 dex and a median value of -1.614 dex spanning 0.44 dex for 68% of the stars with $m_{F625W} < 17$ mag. Further, we identify multiple peaks in the metallicity distribution, indicating different metallicity subgroups.

Additionally, we investigate the chromosome map and its dependences on metallicity. We looked in detail at the most metal-poor group and identified three populations that show a similar spread in [M/H] $\sim$ 0.07 dex while [M/H] increases for higher $\Delta_{F275W,F336W,\,F435W}$.

We also studied the 2D spatial distribution of the [M/H] values and created metallicity maps showing a ring-like structure with higher values, while inside and outside this structure the [M/H] values drop. Finally, we check for metallicity gradients and spatial differences in radial bins for different subgroups of stars. There we find no gradient in [M/H] over our field of view.
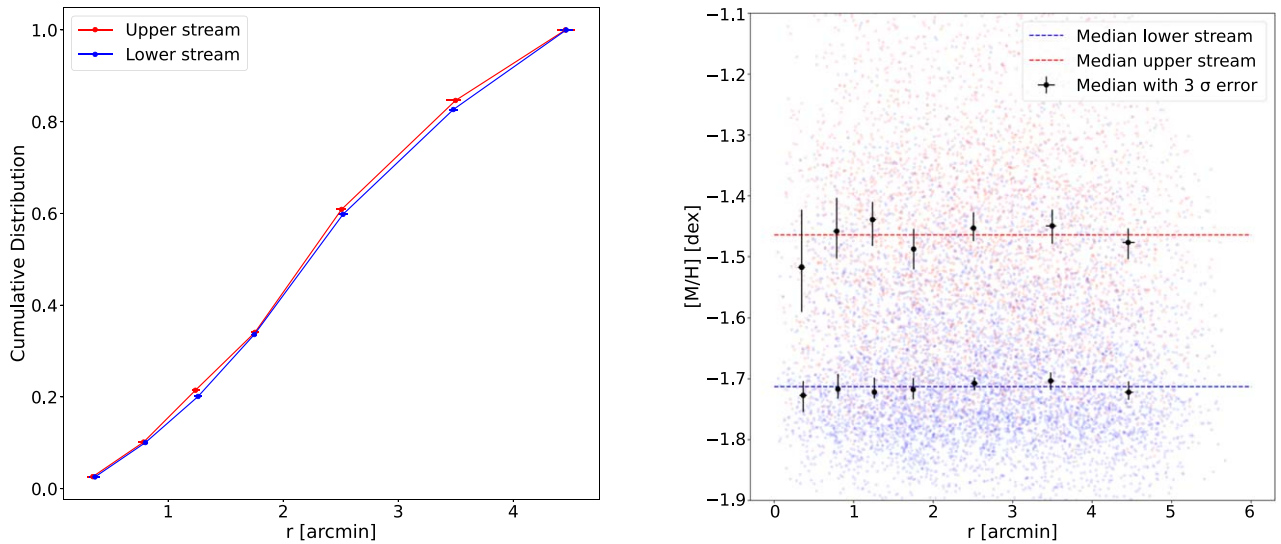
11

Figure 12. Spatial distribution of the two streams in [M/H] vs. $\Delta_{F275W,F814W}$. The left panel shows the cumulative distribution of the two sequences. On the right is their metallicity vs. radius.

Overall, the different [M/H] populations seem to be well mixed and no strong gradient is visible in their radial profiles. However, more information on the abundance might help better separate them and further investigate their differences. In addition, the different subpopulations may be well mixed spatially, but their kinematics may be used to separate them, as it takes longer to erase the stars' memory of their original orbits.

We plan to determine elemental abundances (S. Di Stefano et al. 2024, in preparation; Z. Wang et al. 2024, in preparation), and identify subpopulations and ages (C. Clontz et al. 2024, in preparation). This will bring us closer to uncovering the formation history of ω Cen, the nearest nuclear star cluster.

Appendix A
Completeness

In Paper I we provided the completeness compared to the Anderson & van der Marel (2010) catalog and found that at a magnitude of 18.86 mag in the F625W filter, we have 50% completeness. For our study, we require higher completeness to avoid biases that could cause gradients or spatial variation in metallicity to vary. A magnitude cut of 17 mag gives us over 80% completeness for all fields and even reaches 90% for the majority; see Figure 13 left plot.

To further ensure that we do not bias our sample we check the radial dependence of the magnitude, which should be uniform. Indeed Figure 13 (right) shows that the mean and median values remain constant over our whole field of view, not showing any crowding effects, for the RGB stars.
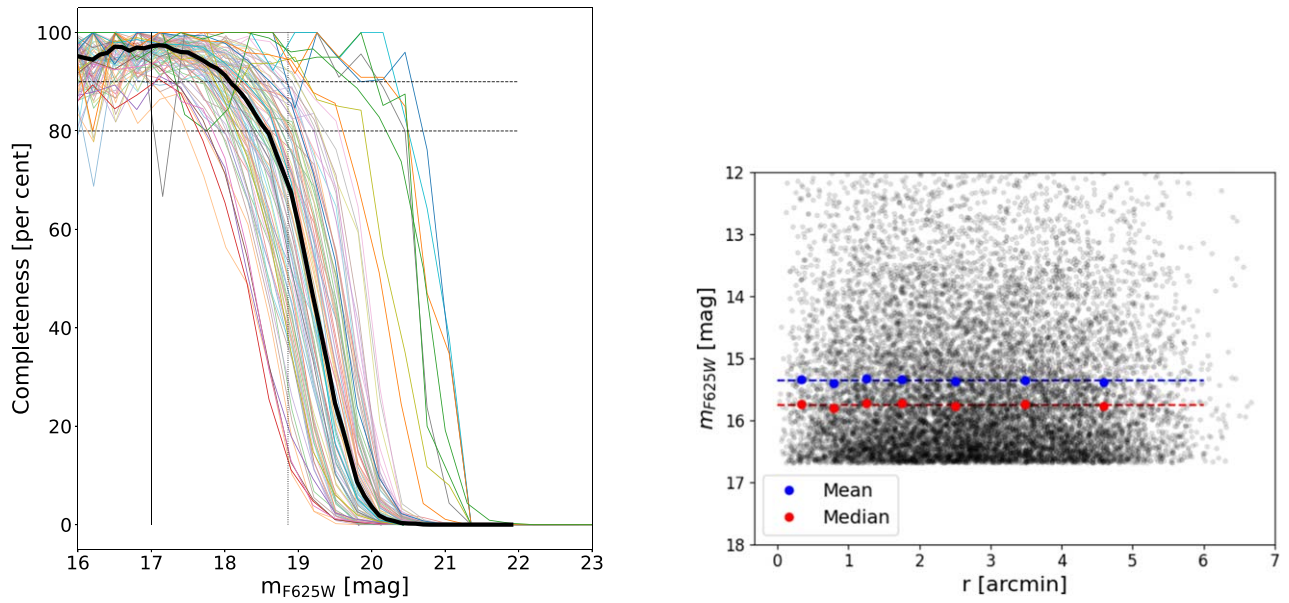
Figure 13. Completeness and magnitude. Left plot: each line shows the completeness fraction of one pointing compared to the HST catalog from Anderson & van der Marel (2010), and the thick black line shows the median completeness fraction. The vertical solid line is at 17 mag and the dotted one at 18.86 mag (for GO 50% completeness on average). The dashed horizontal lines are at 80% and 90%. Right plot: the magnitude of the stars above 17 mag vs. radius, which shows that for our quality cuts, there is no bias or gradient for specific magnitudes.

Appendix B
[M/H] Bias

We noticed a metallicity bias in the different data sets, GO, GTO, and NFM, when using all available magnitudes. In Figure 14 we can see that [M/H] always has a trend to go to higher metallicities for lower SNR, but it differs between data sets. In general, the GTO stars with fainter magnitudes have higher [M/H] and lower SNR than the GO stars, which is likely caused by differences in the observing runs (e.g., different exposure times and numbers of exposures). However, the trend that stars with higher [M/H] have lower SNR is true for all stars and could be because they are redder, on average

fainter (in general, lower SNR), and have more absorption lines that make them look noisier to our spectral fitting routine than more metal-poor stars. When excluding stars fainter than 17 mag in the F625W magnitude we remove most of the stars with SNR $\leqslant 20$ where the bias is visible, making our sample consistent between GTO and GO observations.

Additionally, we check whether the distributions of the stars in GO and GTO are different; see Figure 15. When using all magnitudes the GO distribution is broader, reaching lower metallicities, which would cause the GTO fields always to be on average more metal-rich. However, when applying the magnitude cut the distributions agree well and have no systematic difference.
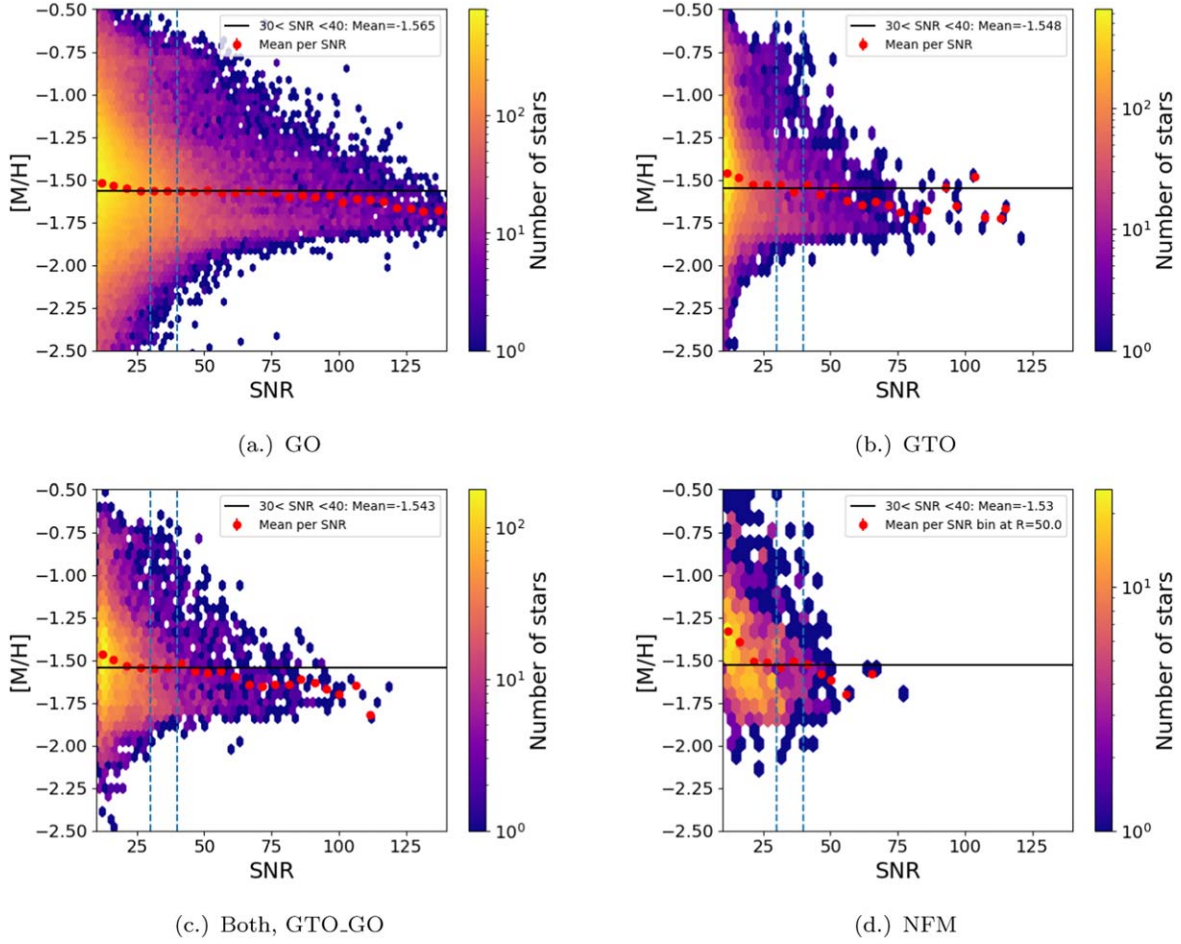
Figure 14. Metallicity bias. We plot the metallicity vs. the SNR for the different data sets underlying our spectroscopic catalog. Red dots are the mean values for each bin and the black solid line is the mean value between SNRs of 30 and 40 (indicated with blue dashed lines).
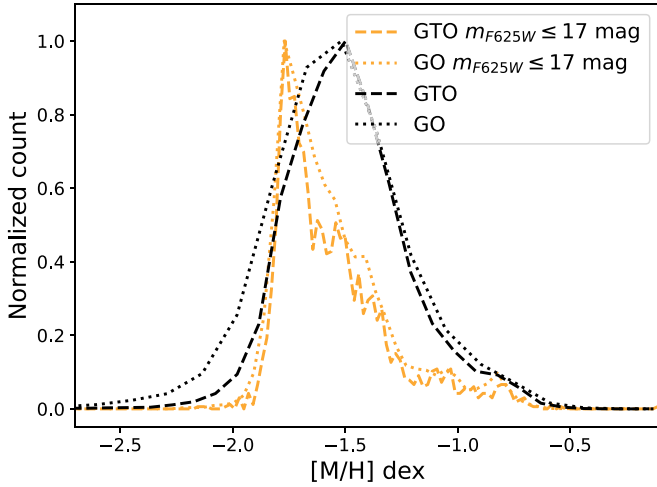

Figure 15. Metallicity distributions of GO and GTO stars. Using all magnitudes the two different data sets have important differences in their distributions. However, with a magnitude cut these disappear and the distributions look almost identical.

Appendix C
Chromosome Map

Since ω Cen is more complex than typical globular clusters, a more elaborate analysis is needed to create a useful chromosome map. Our method is adapted from the procedure described in Milone et al. (2017a).

In summary, one needs more than just two—red and blue—fiducial lines since there are multiple different populations in ω Cen. Hence, one identifies three subsamples: the metal-poor population that also on its own would look like a chromosome map for typical clusters, an intermediate population, and a metal-rich population (Figure 16(a)). The process is iterative and we start by identifying the subsamples in [M/H] first. Metal-poor stars are those belonging to peaks 1, 2, 4, 7, and 11 of the Gaussian mixture model in Section 3.1, metal-rich stars belong to peak 9, and the intermediate population are stars in the six components. We then use slightly adapted fiducial lines from Milone et al. (2017a) to get an initial chromosome map. Next, we identify the subsamples using the different components identified for the [M/H] distribution and also the photometry as in Milone et al. (2017a). Including the photometric information for the subsamples narrows CMD tracks and we calculate new fiducial lines.

The red and blue fiducial lines correspond to the 96th and 4th percentiles in the CMD and pseudo-CMD. In the $m_{F275W} - m_{F814W}$ CMD (Figure 16(b)) the red and blue fiducial lines correspond to the metal-poor population. For the intermediate and rich populations, one needs to find the median fiducial line. In the CMD with the pseudo-color, $C_{F275W,F336W, F435W}$, the populations are more mixed and the intermediate and poor populations can use the same red and
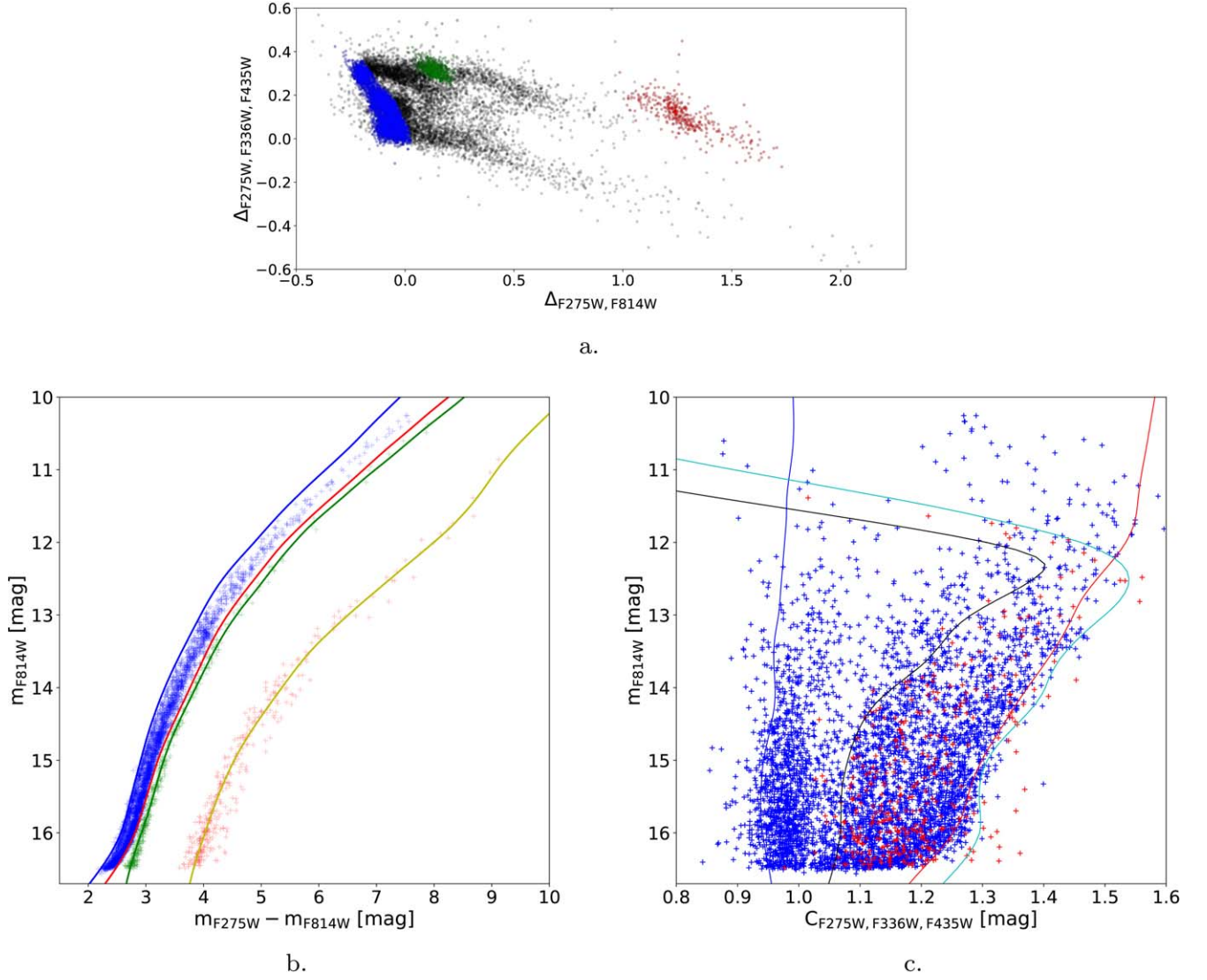
14

a.

b.

c.

Figure 16. The three subsamples used to calculate the chromosome map. (a) The chromosome map of ω Cen, color-coded with [M/H] only for the stars in the three subsamples. (b) The CMD of the subsamples with the fiducial lines for each. Blue and red are the 96th and 4th percentiles for the poor population (blue crosses), green is the median line for the intermediate one (green crosses), and yellow is the median line for the rich population (red crosses). (c) The pseudo-CMD of the subsamples with blue crosses being the poor and intermediate populations and red the rich population. Blue and red lines are the 96% and 4% enclosing lines for the blue crosses, and black and cyan lines are those for the red crosses.

blue fiducial lines, while the metal-rich have different 96th and 4th percentiles indicated with the black and cyan lines (Figure 16(c)). For all fiducial lines, we smoothed and corrected by hand for bright magnitudes.

We repeated this process twice, refining our subsample selection and fiducial lines. Our final fiducial lines are shown in Figure 17 together with the verticalization of the colors for all bright stars.

To get the chromosome map values we calculate the following weights:

$$W_{\mathrm{F275W, F814W_1}}$$
$$= X_{\mathrm{fiducialRed}}(15.5 \text{ mag}) - X_{\mathrm{fiducialBlue}}(15.5 \text{ mag}) \quad (C1)$$

$$W_{\mathrm{F275W, F814W_2}}$$
$$= X_{\mathrm{fiducialOrange}}(15.5 \text{ mag}) - X_{\mathrm{fiducialRed}}(15.5 \text{ mag}) \quad (C2)$$

$$W_{\mathrm{F275W, F814W_3}}$$
$$= X_{\mathrm{fiducialGreen}}(15.5 \text{ mag}) - X_{\mathrm{fiducialOrange}}(15.5 \text{ mag}) \quad (C3)$$

where, e.g., $X_{\mathrm{fiducialRed}}(15.5 \text{ mag})$ is the color of the fiducial line interpolated at magnitude 15.5 in F814W. Then we can find the respective $\Delta_{\mathrm{F275W,F814W_i}}$ values:

$$\Delta_{\mathrm{F275W,F814W_1}} = W_{\mathrm{F275W, F814W_1}} \frac{X - X_{\mathrm{fiducialRed}}}{X_{\mathrm{fiducialRed}} - X_{\mathrm{fiducialBlue}}} \quad (C4)$$

$$\Delta_{\mathrm{F275W,F814W_2}} = W_{\mathrm{F275W,F814W_2}}$$
$$+ W_{\mathrm{F275W,F814W_2}} \frac{X - X_{\mathrm{fiducialOrange}}}{X_{\mathrm{fiducialOrange}} - X_{\mathrm{fiducialRed}}} \quad (C5)$$

$$\Delta_{\mathrm{F275W,F814W_3}} = W_{\mathrm{F275W,F814W_2}} + W_{\mathrm{F275W,F814W_3}}$$
$$+ W_{\mathrm{F275W,F814W_3}} \frac{X - X_{\mathrm{fiducialGreen}}}{X_{\mathrm{fiducialGreen}} - X_{\mathrm{fiducialOrange}}}. \quad (C6)$$

Which of these three $\Delta_{\mathrm{F275W,F814W_i}}$ is used for each star depends on its position relative to the different fiducial lines; see Table 3
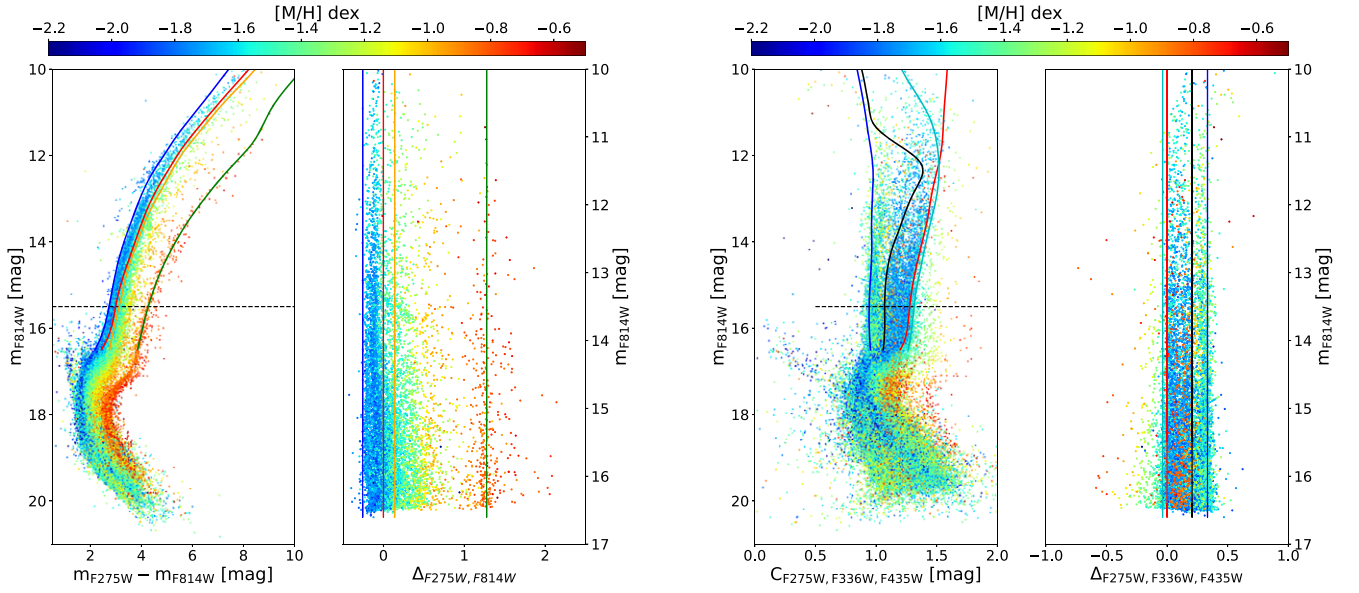
Figure 17. Final fiducial lines. Left: the CMD for all stars; right: the pseudo-CMD. Both are color-coded with [M/H] and show the fiducial lines for the RGB. On the right of each panel is the verticalized CMD, proving that the subsamples do follow these straight lines.

Table 3
Final Chromosome Map Values

Final Chromosome Δ Value	Δ_i Value	Condition
$\Delta_{\mathrm{F275W,F814W}} =$	$\Delta_{\mathrm{F275W,F814W_1}}$, if	$\Delta_{\mathrm{F275W,F814W_1}} \leqslant 0$, right of the red fiducial line
	$\Delta_{\mathrm{F275W,F814W_2}}$, if	$\Delta_{\mathrm{F275W,F814W_1}} > 0$ & $\Delta_{\mathrm{F275W,F814W_2}} \leqslant W_{\mathrm{F275W,F814W_2}}$, between red and orange fiducial lines
	$\Delta_{\mathrm{F275W,F814W_3}}$, if	$\Delta_{\mathrm{F275W,F814W_3}} > W_{\mathrm{F275W,F814W_2}}$, right of the orange fiducial line
$\Delta_{\mathrm{F275W,F336W,F435W}} =$	$\Delta_{\mathrm{F275W,F336W,F435W_1}}$, if	star does not belong to the most metal-rich peak ($\neq$ index 9)
	$\Delta_{\mathrm{F275W,F336W,F435W_2}}$, if	star belongs to metal-rich peak (= index 9)

Note. The metal-rich peak (index 9) is taken from the Gaussian mixture model (Table 2 in Section 3.1).

for details. For the $\Delta_{\mathrm{F275W,F336W,F435W}}$ value we calculate

$$W_{\mathrm{F275W,F336W,F435W_1}} = Y_{\mathrm{fiducialRed}}(15.5 \text{ mag}) - Y_{\mathrm{fiducialBlue}}(15.5 \text{ mag}) \quad (C7)$$

$$W_{\mathrm{F275W,F336W,F435W_2}} = Y_{\mathrm{fiducialRed}}(15.5 \text{ mag}) - Y_{\mathrm{fiducialCyan}}(15.5 \text{ mag}) \quad (C8)$$

$$W_{\mathrm{F275W,F336W,F435W_3}} = Y_{\mathrm{fiducialCyan}}(15.5 \text{ mag}) - Y_{\mathrm{fiducialBlack}}(15.5 \text{ mag}) \quad (C9)$$

and then

$$\Delta_{\mathrm{F275W,F336W,F435W_1}} = W_{\mathrm{F275W,F336W,F435W_1}} \frac{Y_{\mathrm{fiducialRed}} - Y}{Y_{\mathrm{fiducialRed}} - Y_{\mathrm{fiducialBlue}}} \quad (C10)$$

$$\Delta_{\mathrm{F275W,F336W,F435W_2}} = W_{\mathrm{F275W,F336W,F435W_2}} + W_{\mathrm{F275W,F336W,F435W_3}} \frac{Y_{\mathrm{fiducialCyan}} - Y}{Y_{\mathrm{fiducialCyan}} - Y_{\mathrm{fiducialBlack}}}. \quad (C11)$$

Depending on each metallicity, each star gets assigned either $\Delta_{\mathrm{F275W,F336W,F435W_1}}$ or $\Delta_{\mathrm{F275W,F336W,F435W_2}}$. The condition is described in Table 3.

Finally, we color-coded the final chromosome map with all the components of the Gaussian mixture model of the [M/H] distribution (Section 3.1) in Figure 18. All the components are at specific locations on the map depending on their [M/H], thus separating different subpopulations and showing the complexity of the clusters.
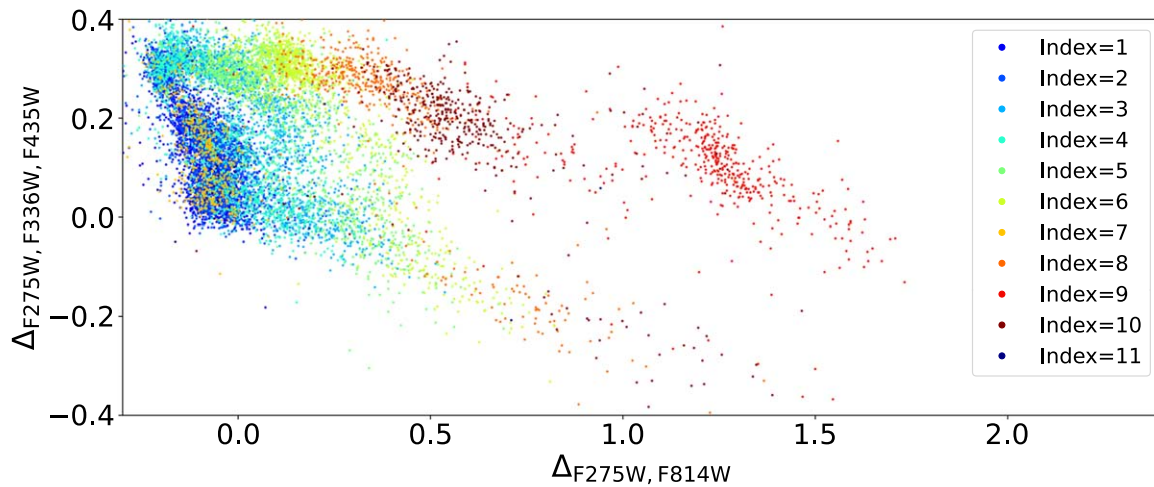
Figure 18. Chromosome map color-coded with the subgroups identified in the metallicity distribution. We use the components of the multi-Gaussian mixture model used in Section 3.1 and color-code the stars in the chromosome map with the component (index) they most likely belong to.

ORCID iDs

M. S. Nitschai ⓘ https://orcid.org/0000-0002-2941-4480
N. Neumayer ⓘ https://orcid.org/0000-0002-6922-2598
M. Häberle ⓘ https://orcid.org/0000-0002-5844-4443
C. Clontz ⓘ https://orcid.org/0009-0005-8057-0031
A. C. Seth ⓘ https://orcid.org/0000-0003-0248-5470
A. P. Milone ⓘ https://orcid.org/0000-0001-7506-930X
M. Alfaro-Cuello ⓘ https://orcid.org/0000-0002-1212-2844
A. Bellini ⓘ https://orcid.org/0000-0003-3858-637X
S. Dreizler ⓘ https://orcid.org/0000-0001-6187-5941
A. Feldmeier-Krause ⓘ https://orcid.org/0000-0002-0160-7221
T.-O. Husser ⓘ https://orcid.org/0000-0003-2466-5077
S. Kamann ⓘ https://orcid.org/0000-0001-6604-0505
M. Latour ⓘ https://orcid.org/0000-0002-7547-6180
M. Libralato ⓘ https://orcid.org/0000-0001-9673-7397
G. van de Ven ⓘ https://orcid.org/0000-0003-4546-7731
K. Voggel ⓘ https://orcid.org/0000-0001-6215-0950
Z. Wang ⓘ https://orcid.org/0000-0003-2512-6892

References

Alfaro-Cuello, M., Kacharov, N., Neumayer, N., et al. 2019, ApJ, 886, 57
Alfaro-Cuello, M., Kacharov, N., Neumayer, N., et al. 2020, ApJ, 892, 20
Alvarez Garay, D. A., Mucciarelli, A., Bellazzini, M., Lardo, C., & Ventura, P. 2024, A&A, 681, A54
Anderson, A. J. 1997, PhD thesis, University of California, Berkeley
Anderson, J., & van der Marel, R. P. 2010, ApJ, 710, 1032
Astropy Collaboration, Price-Whelan, A. M., Lim, P. L., et al. 2022, ApJ, 935, 167
Astropy Collaboration, Price-Whelan, A. M., Sipőcz, B. M., et al. 2018, AJ, 156, 123
Astropy Collaboration, Robitaille, T. P., Tollerud, E. J., et al. 2013, A&A, 558, A33
Bacon, R., Accardo, M., Adjali, L., et al. 2010, Proc. SPIE, 7735, 773508
Bacon, R., Vernet, J., Borisova, E., et al. 2014, Msngr, 157, 13
Bastian, N., & Lardo, C. 2018, ARA&A, 56, 83
Baumgardt, H., & Hilker, M. 2018, MNRAS, 478, 1520
Baumgardt, H., & Vasiliev, E. 2021, MNRAS, 505, 5957
Bedin, L. R., Piotto, G., Anderson, J., et al. 2004, ApJL, 605, L125
Bellini, A., Anderson, J., Bedin, L. R., et al. 2017a, ApJ, 842, 6
Bellini, A., Anderson, J., van der Marel, R. P., et al. 2014, ApJ, 797, 115
Bellini, A., Bedin, L. R., Piotto, G., et al. 2010, AJ, 140, 631
Bellini, A., Libralato, M., Bedin, L. R., et al. 2018, ApJ, 853, 86
Bellini, A., Milone, A. P., Anderson, J., et al. 2017b, ApJ, 844, 164
Bellini, A., Piotto, G., Bedin, L. R., et al. 2009, A&A, 507, 1393
Calamida, A., Strampelli, G., Rest, A., et al. 2017, AJ, 153, 175
Calamida, A., Zocchi, A., Bono, G., et al. 2020, ApJ, 891, 167
Callingham, T. M., Cautun, M., Deason, A. J., et al. 2022, MNRAS, 513, 4107
Caswell, T. A., Lee, A., Sales de Andrade, E., et al. 2023, matplotlib/matplotlib: REL: v3.7.1, Zenodo, doi:10.5281/zenodo.7697899
Cappellari, M., McDermid, R. M., Alatalo, K., et al. 2013, MNRAS, 432, 1862
Elson, R. A. W., Gilmore, G. F., Santiago, B. X., & Casertano, S. 1995, AJ, 110, 682
Freeman, K. C., & Rodgers, A. W. 1975, ApJL, 201, L71
Georgiev, I. Y., & Böker, T. 2014, MNRAS, 441, 3570
Geyer, E. H., Hopp, U., & Nelles, B. 1983, A&A, 125, 359
Häberle, M., Neumayer, N., Bellini, A., et al. 2024a, arXiv:2404.03722
Häberle, M., Neumayer, N., Seth, A., et al. 2024b, arXiv:2405.06015
Harris, C. R., Millman, K. J., van der Walt, S. J., et al. 2020, Natur, 585, 357
Harris, W. E. 2010, arXiv:1012.3224
Helmi, A., Babusiaux, C., Koppelman, H. H., et al. 2018, Natur, 563, 85
Hilker, M., Kayser, A., Richtler, T., & Willemsen, P. 2004, A&A, 422, L9
Hoyer, N., Neumayer, N., Georgiev, I. Y., Seth, A. C., & Greene, J. E. 2021, MNRAS, 507, 3246
Hunter, J. D. 2007, CSE, 9, 90
Husser, T.-O., Kamann, S., Dreizler, S., et al. 2016, A&A, 588, A148
Husser, T.-O., Latour, M., Brinchmann, J., et al. 2020, A&A, 635, A114
Husser, T. O., Wende-von Berg, S., Dreizler, S., et al. 2013, A&A, 553, A6
Ibata, R., Malhan, K., Tenachi, W., et al. 2024, ApJ, 967, 89
Ibata, R. A., Bellazzini, M., Malhan, K., Martin, N., & Bianchini, P. 2019, NatAs, 3, 667
Ibata, R. A., Gilmore, G., & Irwin, M. J. 1994, Natur, 370, 194
Ibata, R. A., Wyse, R. F. G., Gilmore, G., Irwin, M. J., & Suntzeff, N. B. 1997, AJ, 113, 634
Johnson, C. I., Dupree, A. K., Mateo, M., et al. 2020, AJ, 159, 254
Johnson, C. I., & Pilachowski, C. A. 2010, ApJ, 722, 1373
Joo, S.-J., & Lee, Y.-W. 2013, ApJ, 762, 36
Kacharov, N., Alfaro-Cuello, M., Neumayer, N., et al. 2022, ApJ, 939, 118
Kacharov, N., Neumayer, N., Seth, A. C., et al. 2018, MNRAS, 480, 1973
Kamann, S., Giesers, B., Bastian, N., et al. 2020, A&A, 635, A65
Kamann, S., Husser, T. O., Dreizler, S., et al. 2018, MNRAS, 473, 5591
Kamann, S., Wisotzki, L., & Roth, M. M. 2013, A&A, 549, A71
Kruijssen, J. M. D., Pfeffer, J. L., Reina-Campos, M., Crain, R. A., & Bastian, N. 2019, MNRAS, 486, 3180
Laporte, C. F. P., Johnston, K. V., Gómez, F. A., Garavito-Camargo, N., & Besla, G. 2018, MNRAS, 481, 286
Latour, M., Calamida, A., Husser, T. O., et al. 2021, A&A, 653, L8
Lee, Y. W., Joo, J. M., Sohn, Y. J., et al. 1999, Natur, 402, 55
Libralato, M., Bellini, A., van der Marel, R. P., et al. 2018, ApJ, 861, 99
Libralato, M., Bellini, A., Vesperini, E., et al. 2022, ApJ, 934, 150
Limberg, G., Souza, S. O., Pérez-Villegas, A., et al. 2022, ApJ, 935, 109
Lovisi, L., Mucciarelli, A., Dalessandro, E., Ferraro, F. R., & Lanzoni, B. 2013, ApJ, 778, 64
Majewski, S. R., Nidever, D. L., Smith, V. V., et al. 2012, ApJL, 747, L37
Marigo, P., Girardi, L., Bressan, A., et al. 2017, ApJ, 835, 77
Marino, A. F., Milone, A. P., Renzini, A., et al. 2019a, MNRAS, 487, 3815
Marino, A. F., Milone, A. P., Sills, A., et al. 2019b, ApJ, 887, 91
Martins, F., Morin, J., Charbonnel, C., Lardo, C., & Chantereau, W. 2020, A&A, 635, A52

Massari, D., Koppelman, H. H., & Helmi, A. 2019, A&A, 630, L4

Mayor, M., Duquennoy, A., Udry, S., Andersen, J., & Nordstrom, B. 1996, in ASP Conf. Ser. 90, The Origins, Evolution, and Destinies of Binary Stars in Clusters, ed. E. F. Milone & J. C. Mermilliod (San Francisco, CA: ASP), 190

McKinney, W. 2010, in Proc. 9th Python in Science Conf., ed. S. van der Walt & J. Millman (Austin, TX: SciPy), 56

Mészáros, S., Masseron, T., Fernández-Trincado, J. G., et al. 2021, MNRAS, 505, 1645

Milone, A. P., Marino, A. F., Bedin, L. R., et al. 2017a, MNRAS, 469, 800

Milone, A. P., Marino, A. F., Piotto, G., et al. 2015a, MNRAS, 447, 927

Milone, A. P., Marino, A. F., Piotto, G., et al. 2015b, ApJ, 808, 51

Milone, A. P., Marino, A. F., Renzini, A., et al. 2018, MNRAS, 481, 5098

Milone, A. P., Marino, A. F., Renzini, A., et al. 2020, MNRAS, 497, 3846

Milone, A. P., Piotto, G., Bedin, L. R., et al. 2012, ApJ, 744, 58

Milone, A. P., Piotto, G., Renzini, A., et al. 2017b, MNRAS, 464, 3636

Nitschai, M., Neumayer, N., Clontz, C., et al. 2023, ApJ, 958, 8

Neumayer, N., Seth, A., & Böker, T. 2020, A&ARv, 28, 4

Norris, J. E. 2004, ApJL, 612, L25

Pancino, E., Ferraro, F. R., Bellazzini, M., Piotto, G., & Zoccali, M. 2000, ApJL, 534, L83

Pancino, E., Seleznev, A., Ferraro, F. R., Bellazzini, M., & Piotto, G. 2003, MNRAS, 345, 683

pandas development team, T. 2020, pandas-dev/pandas: Pandas, v1.5.3, Zenodo, doi:10.5281/zenodo.7549438

Pechetti, R., Kamann, S., Krajnovic, D., et al. 2024, MNRAS, 528, 4941

Pedregosa, F., Varoquaux, G., Gramfort, A., et al. 2011, J. Machine Learning Res., 12, 2825

Pfeffer, J., Griffen, B. F., Baumgardt, H., & Hilker, M. 2014, MNRAS, 444, 3670

Pfeffer, J., Lardo, C., Bastian, N., Saracino, S., & Kamann, S. 2021, MNRAS, 500, 2514

Piotto, G., Milone, A. P., Bedin, L. R., et al. 2015, AJ, 149, 91

Piotto, G., Villanova, S., Bedin, L. R., et al. 2005, ApJ, 621, 777

Sánchez-Janssen, R., Côté, P., Ferrarese, L., et al. 2019, ApJ, 878, 18

Schlafly, E. F., & Finkbeiner, D. P. 2011, ApJ, 737, 103

Seth, A. C., Dalcanton, J. J., Hodge, P. W., & Debattista, V. P. 2006, AJ, 132, 2539

Sollima, A., Ferraro, F. R., Bellazzini, M., et al. 2007, ApJ, 654, 915

Sollima, A., Ferraro, F. R., Pancino, E., & Bellazzini, M. 2005, MNRAS, 357, 265

Tailo, M., Di Criscienzo, M., D'Antona, F., Caloi, V., & Ventura, P. 2016, MNRAS, 457, 4525

Ting, Y.-S., Rix, H.-W., Conroy, C., Ho, A. Y. Q., & Lin, J. 2017, ApJL, 849, L9

van de Ven, G., van den Bosch, R. C. E., Verolme, E. K., & de Zeeuw, P. T. 2006, A&A, 445, 513

Villanova, S., Piotto, G., King, I. R., et al. 2007, ApJ, 663, 296

Virtanen, P., Gommers, R., Oliphant, T. E., et al. 2020, NatMe, 17, 261

Walcher, C. J., Böker, T., Charlot, S., et al. 2006, ApJ, 649, 692

Walcher, C. J., van der Marel, R. P., McLaughlin, D., et al. 2005, ApJ, 618, 237

Willman, B., & Strader, J. 2012, AJ, 144, 76

Wragg, F., Kamann, S., Saracino, S., et al. 2024, MNRAS, in press

Xiang, M., Ting, Y.-S., Rix, H.-W., et al. 2019, ApJS, 245, 34